

IN SITU RAMAN SPECTROSCOPY OF PRESSURE-INDUCED
PHASE TRANSFORMATIONS IN DyPO_4 AND $\text{Gd}_x\text{Dy}_{(1-x)}\text{PO}_4$

by

Matthew Anthony Musselman

A thesis submitted to the Faculty and the Board of Trustees of the Colorado School of Mines in partial fulfillment of the requirements for the degree of Master of Science (Materials Science).

Golden, Colorado

Date _____

Signed: _____

Matthew Anthony Musselman

Signed: _____

Dr. Corinne Packard
Thesis Advisor

Golden, Colorado

Date _____

Signed: _____

Dr. Ryan O'Hayre
Program Manager
Materials Science

ABSTRACT

Xenotime DyPO_4 and $\text{Gd}_x\text{Dy}_{(1-x)}\text{PO}_4$ ($x = 0.4, 0.5, 0.6$) (tetragonal $I4_1/amd$ zircon structure) have been studied at ambient temperature under high pressures inside a diamond anvil cell with *in situ* Raman spectroscopy. The Raman active modes of the xenotime structure were observed at low pressures and the appearance of new Raman peaks at higher pressures indicate a phase transformation to a lower symmetry structure, likely monoclinic. The onset phase transformation pressure of DyPO_4 was 15.3 GPa. The transformation pressures of the solid solutions ($\text{Gd}_x\text{Dy}_{(1-x)}\text{PO}_4$) were 12.2 GPa (40/60, $x=0.4$), 10.1 GPa (50/50, $x=0.5$), and 11.9 GPa (60/40, $x=0.6$). The addition of Gd resulted in a decrease in transformation pressure from pure DyPO_4 . A line crossing as a result of Raman mode softening is observed at approximately 7-8 GPa for each material, preceding the phase transformation. DyPO_4 underwent a reversible phase transformation and returned to the xenotime phase after decompression. The solid solutions yielded partially reversible phase transformations and retained peaks from the high-pressure phase while reforming xenotime peaks upon decompression.

TABLE OF CONTENTS

ABSTRACT.....	iii
LIST OF FIGURES	vi
LIST OF TABLES.....	viii
ACKNOWLEDGEMENTS.....	ix
CHAPTER 1 INTRODUCTION.....	1
1.1 Rare-Earth Orthophosphates (REPO ₄)	1
1.2 Ceramic Matrix Composites (CMCs).....	3
1.3 Pressure-Induced Phase Transformations.....	7
1.4 Research Overview.....	8
CHAPTER 2 EXPERIMENTAL METHODS	10
2.1 Materials Synthesis.....	10
2.2 Phase Analysis and Thermal Behavior.....	11
2.2.1 X-Ray Diffraction (XRD).....	11
2.2.2 Differential Thermal Analysis (DTA)/Thermogravimetric Analysis (TGA)	15
2.2.3 Thermal Behavior Comparison	18
2.3 Scanning Electron Microscopy (SEM)/Energy Dispersive X-Ray Spectroscopy(EDS). 18	
2.4 Diamond Anvil Cell (DAC) with <i>in situ</i> Raman Spectroscopy.....	21
2.5 Data Analysis.....	24
CHAPTER 3 RESEARCH PAPER: <i>IN-SITU</i> RAMAN SPECTROSCOPY OF PRESSURE-INDUCED PHASE TRANSFORMATIONS IN DyPO ₄ AND Gd _x Dy _(1-x) PO ₄	26
3.1 Manuscript – Abstract	26
3.2 Manuscript – Introduction	27
3.3 Manuscript – Experimental Methods	29

3.4 Manuscript – Results and Discussion.....	31
3.5 Manuscript – Conclusion.....	41
3.6 Manuscript – Acknowledgements	42
CHAPTER 4 CONCLUSIONS AND FUTURE WORK.....	43
REFERENCES CITED.....	45

LIST OF FIGURES

Figure 1.1:	Projections down [001] of the monazite and xenotime structures generated from 3-D models created in VESTA. The PO ₄ tetrahedra are purple and the rare-earth polyhedra are yellow (monazite) and blue (xenotime).....	2
Figure 1.2:	Lanthanide elements labeled with the thermodynamically stable structure as REPO ₄ s.	2
Figure 1.3:	Optical micrographs showing crack interactions with sapphire fibers in an alumina matrix [21]. The image on the left has a monazite LaPO ₄ coating. The image on the left is uncoated.	4
Figure 1.4:	SEM image of monazite coated fiber after indentation push-out test [21].	6
Figure 1.5:	Compiled experimental phase transformation pressures of xenotime REPO ₄ (RE ionic radii based on eight-fold coordination of the xenotime structure).	8
Figure 2.1:	TbPO ₄ XRD Incremental Heat Treatments.....	12
Figure 2.2:	Gd _{0.6} Dy _{0.4} PO ₄ XRD Incremental Heat Treatments.....	13
Figure 2.3:	Gd _{0.5} Dy _{0.5} PO ₄ XRD Incremental Heat Treatments.....	13
Figure 2.4:	Gd _{0.4} Dy _{0.6} PO ₄ XRD Incremental Heat Treatments.....	14
Figure 2.5:	DyPO ₄ XRD Incremental Heat Treatments	14
Figure 2.6:	DTA/TGA data of TbPO ₄ after synthesis	15
Figure 2.7:	DTA/TGA data of Gd _{0.6} Dy _{0.4} PO ₄ after synthesis	16
Figure 2.8:	DTA/TGA data of Gd _{0.5} Dy _{0.5} PO ₄ after synthesis	16
Figure 2.9:	DTA/TGA data of Gd _{0.4} Dy _{0.6} PO ₄ after synthesis	17
Figure 2.10:	DTA/TGA data of DyPO ₄ after synthesis.....	17
Figure 2.11:	SEM image of TbPO ₄ as precipitated	19
Figure 2.12:	SEM image of Gd _{0.6} Dy _{0.4} PO ₄ as precipitated	19
Figure 2.13:	SEM image of Gd _{0.5} Dy _{0.5} PO ₄ as precipitated	20
Figure 2.14:	SEM image of Gd _{0.4} Dy _{0.6} PO ₄ as precipitated	20
Figure 2.15:	SEM image of DyPO ₄ as precipitated.....	21

Figure 2.16:	Raman spectra of anhydrite (CaSO_4) and xenotime (DyPO_4)	23
Figure 2.17:	Raman spectra of xenotime (DyPO_4) and ruby fluorescence at atmospheric pressure	24
Figure 2.18:	Lorentzian function (red) fit to a DyPO_4 Raman spectrum (blue).....	25
Figure 2.19:	Peak locations from Lorentzian analysis (red) overlaid with the DyPO_4 Raman spectrum (blue).	25
Figure 3.1:	Selected Raman spectra of TbPO_4 (a), $\text{Gd}_{0.6}\text{Dy}_{0.4}\text{PO}_4$ (b), $\text{Gd}_{0.5}\text{Dy}_{0.5}\text{PO}_4$ (c), $\text{Gd}_{0.4}\text{Dy}_{0.6}\text{PO}_4$ (d), and DyPO_4 (e) during compression. Peaks associated with the onset of the phase transformation are indicated by *	33
Figure 3.2:	Raman modes as a function of pressure during compression. Initial xenotime phase modes are shown in black and new high-pressure phase modes are shown in red. At the onset of transformation a mostly full set of peaks appear...35	
Figure 3.3:	Experimental transformation pressures and line crossing pressures of xenotime REPO_4s measured in this study.....	36
Figure 3.4:	Experimental transformation pressures of xenotime REPO_4s from this study and previous studies	38
Figure 3.5:	Decompression Raman spectra of TbPO_4 (a), $\text{Gd}_{0.6}\text{Dy}_{0.4}\text{PO}_4$ (b), $\text{Gd}_{0.5}\text{Dy}_{0.5}\text{PO}_4$ (c), $\text{Gd}_{0.4}\text{Dy}_{0.6}\text{PO}_4$ (d), and DyPO_4 (e).....	40

LIST OF TABLES

Table 2.1:	RE ratios in solid solutions measured by EDS.	21
Table 3.1:	Xenotime Raman modes and slopes table of TbPO ₄ , DyPO ₄ , and Gd _x Dy _(1-x) PO ₄ solid solutions compared to those for TbPO ₄ , reported by Tatsi <i>et al.</i> [35].	36
Table 3.2:	Summary of experimental results for phase transformation pressures and line crossings. Errors reported are the resolutions of pressure increments indicating the previous pressure before transformation. (*Effective rare-earth radii of solid solutions are linear interpolations between the radii of Gd and Dy)	38

ACKNOWLEDGEMENTS

This research has been a result of encouragement and support from many people throughout the years. Thank you to the National Science Foundation for their funding of this research project under award number DMR-1352499. Thank you to the Metallurgical and Materials Engineering Department, a group of people that have guided me throughout my research and academics. Many thanks to Dr. Bianca Haberl whose experience and knowledge enriched the quality of my research. Her contribution has been invaluable. I appreciate the support and motivation from my committee members, Dr. Ivar Reimanis and Dr. Geoff Brennecka. I would especially like to thank my advisor, Dr. Corinne Packard, who gave me this opportunity. Her guidance throughout my time in her research group has influenced me to be a stronger and well-rounded scientist. I appreciate the help and experience I received from fellow students whose friendship and knowledge I value greatly. I am thankful for my friends and family who have stood by me throughout my pursuits.

CHAPTER 1 INTRODUCTION

Rare-earth orthophosphates (REPO_4) are ceramic materials with applications that utilize their chemical, optical, magnetic, and mechanical properties. They are naturally occurring minerals commonly found in geological deposits of rare-earth elements. This chapter discusses the structures and applications of REPO_4 s, specifically their use as fiber coatings in ceramic matrix composites (CMCs). Fiber composites are introduced and the relevant toughening mechanisms during fracture are explained. The high-pressure behavior of xenotime REPO_4 s is reviewed and summarized. This chapter motivates the necessity for high-pressure research of REPO_4 s to better understand the relationship between phase transformation pressure and the performance of CMC fiber coatings. Finally, this chapter will describe the layout of this thesis and the content covered in each chapter.

1.1 Rare-Earth Orthophosphates (REPO_4)

Anhydrous REPO_4 s crystallize into either the xenotime structure (tetragonal, $I4_1/amd$) or the monazite structure (monoclinic, $P2_1/n$) under ambient conditions depending on the radius of the rare-earth cation. Orthophosphates with heavy, smaller rare-earths (RE) (Tb to Lu) are more thermodynamically stable in the xenotime structure while orthophosphates with light, larger RE's (La to Gd) are most stable in the monazite structure [1, 2]. Xenotime has ~5% larger molar volume than monazite [3, 4]. Figure 1.1 displays 2-D projections of the monazite and xenotime structures. The coordination number of rare-earth cations varies between the two phases. Monazite has a nine-fold coordination with adjacent oxygen atoms and xenotime has eight-fold coordination [3]. Transformation from one phase to the other requires the breaking and reforming of bonds. Figure 1.2 shows how lanthanide elemental REPO_4 s separate into their

thermodynamically stable structures at ambient temperature and pressure. Compounds containing RE's near the monazite-xenotime boundary have been observed to crystallize into either phase or a combination of both through varied processing conditions. For example, metastable monazite has been observed in DyPO₄ and TbPO₄, transitioning to xenotime at elevated temperatures [5]. These RE's are highlighted in Figure 1.1 as the polymorphic range. These REPO₄s are of particular interest due to their relative ease in assuming metastable phases.

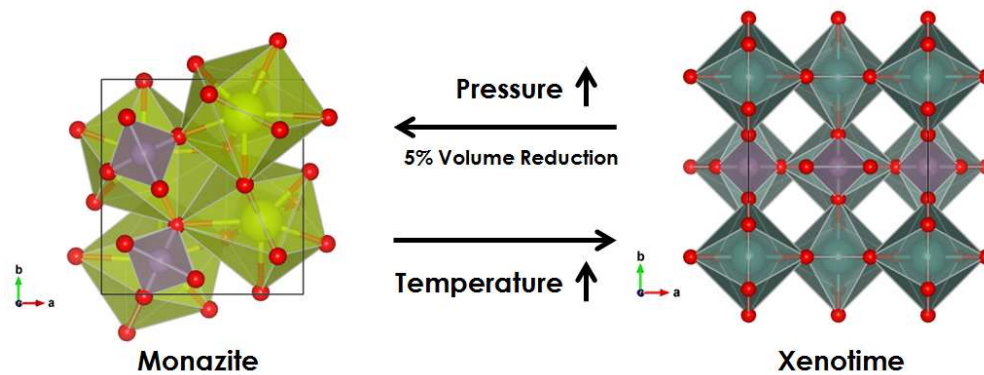


Figure 1.1: Projections down [001] of the monazite and xenotime structures generated from 3-D models created in VESTA. The PO₄ tetrahedra are purple and the rare-earth polyhedra are yellow (monazite) and blue (xenotime).

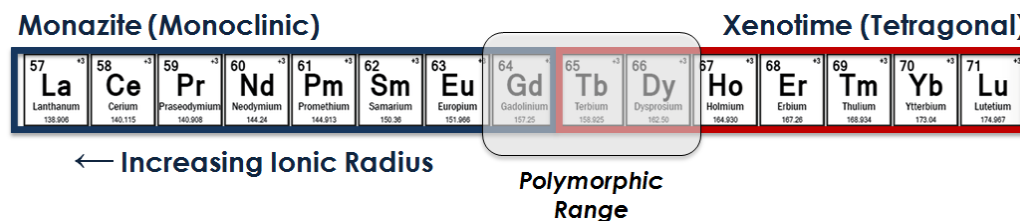


Figure 1.2: Lanthanide elements labeled with the thermodynamically stable structure as REPO₄s.

Both phases of REPO₄s are non-oxidizing ceramics that plastically deform more easily than other oxides with similar melting temperatures (~2000 °C). They have been utilized in a

variety of applications, making use of their mechanical, chemical, and optical properties. Much of the prior research into REPO₄s focused on solid state radioactive waste storage due to desirable chemical properties [6-10]. The solubility of radioactive actinides into REPO₄ structures, REPO₄s insolubility in water, and self-healing properties upon taking radiation damage make these materials an ideal host for containment. Thermal coatings of REPO₄s provide chemically-resistant barriers with low thermal conductivity [11, 12]. Their optical and luminescent properties have also been researched for optoelectronic applications such as lasers and scintillators [13-15]. More recently, REPO₄ mechanical properties have been investigated to enhance ceramic toughening mechanisms. These rare-earth compounds remain chemically stable at elevated temperatures among typical structural ceramics (such as alumina) and have shown potential as fiber coatings in oxide-oxide ceramic matrix composites.

1.2 Ceramic Matrix Composites (CMCs)

CMCs are material systems that incorporate dispersed ceramic particles or fibers into a ceramic matrix. Due to the brittle nature of ceramics these structures are commonly introduced to increase fracture toughness through a variety of mechanisms that impede or deflect crack propagation. Cracks follow the path of least resistance in bulk material, which is the direction of maximum tensile stress. At the interface between the fiber and the matrix, the interfacial bonds are often the weakest and easiest to break and so the crack deflects along the interface. For example, a crack propagating through the matrix that intersects with a particle or fiber would be redirected around the dispersed phase. Deflecting the crack along a longer path consumes more energy than it would have otherwise, thereby increasing the fracture toughness of the material system.

Alumina (Al_2O_3) is a major structural ceramic and has been thoroughly investigated in CMC fiber systems where both the fiber and the matrix are alumina [16-18]. Using the same material for both the matrix and fibers avoids coefficient of thermal expansion (CTE) mismatch that can generate internal stress fields during temperature fluctuations and processing. However, a homogenous CMC creates a strongly bonded interface between the matrix and the fiber, which inhibits crack deflection along that interface and forces the crack propagation directly through the fiber. This drawback impedes the increased fracture toughness that CMC systems aim to achieve. The application of another material as a fiber coating, such as REPO_4 , has been shown to deflect crack propagation along the interface between the coating and fiber/matrix [16-21]. Figure 1.3 shows optical micrographs of crack propagation in alumina/alumina fiber composites demonstrating ideal crack deflection with a monazite LaPO_4 coating and failed crack deflection in an uncoated fiber. An ideal coating will be chemically non-reactive with the CMC material and remain stable under the conditions of the intended application, such as high temperature. As previously mentioned, REPO_4 s are non-oxidizing and stable at high temperatures.

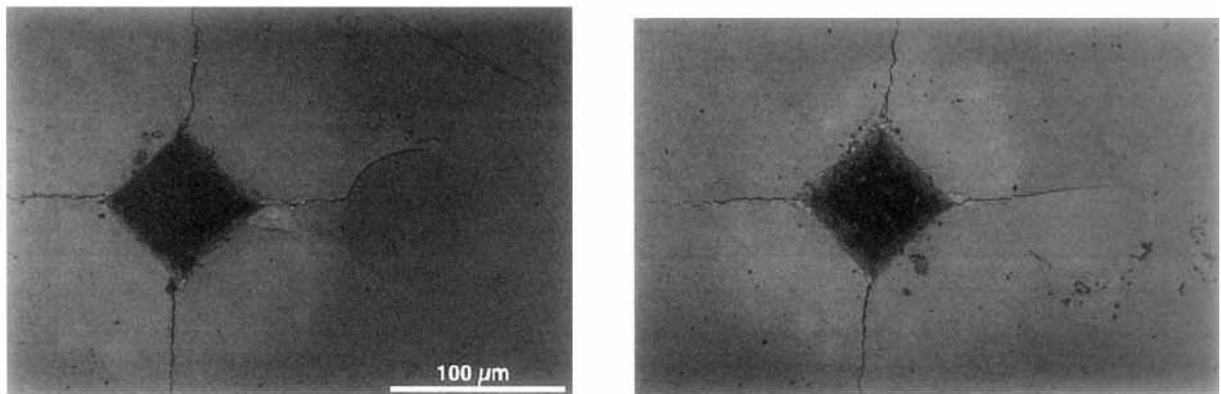


Figure 1.3: Optical micrographs showing crack interactions with sapphire fibers in an alumina matrix [21]. The image on the left has a monazite LaPO_4 coating. The image on the right is uncoated.

Fiber sliding within the matrix is another mechanism that increases the toughness and strength of CMC fiber systems [22-25]. This toughening mechanism shields the crack tip by bridging fibers across the crack generating compressive stresses which hinder further crack propagation, putting the fibers in tension. As the crack extends it also expands generating increased stresses on the fibers that grow large enough to induce fracture and then failure of the fibers. Rather than loading the fibers to the point the fracture, the coating allows the fibers to slide within the matrix before reaching their critical fracture stress. There are many factors that influence fiber sliding such as interfacial roughness of the fiber and deformation mechanisms of the coating [26-28]. Monazite LaPO_4 fiber coatings have been shown to promote fiber sliding due to debonding and its relative ease to plastically deform via microfracture, dislocation slip, cataclastic flow, and twinning [21, 27]. While extensive damage was observed in the softer LaPO_4 coatings, the relatively harder fibers were undamaged. Although fiber sliding was observed, the fiber push-out stresses were significantly higher than other CMC systems. LaPO_4 fiber coatings had fiber push-out stresses measured at 70 – 200 MPa [21, 27, 28]. This range is relatively high compared to more preferable boron nitride interfaces in SiC CMCs which measured 5 – 80 MPa push-out stresses [26, 29, 30]. Figure 1.4 shows an image of a LaPO_4 coated fiber after a push-out test using nanoindentation.

Further investigations into other REPO_4 s as fiber coatings sought to decrease the fiber sliding stress. Experimental testing of xenotime DyPO_4 fiber coatings demonstrated similar push-out stresses as monazite LaPO_4 . But a xenotime solid solution of Gd and Dy produced lower fiber push-out stresses than DyPO_4 and LaPO_4 . $\text{Gd}_{0.4}\text{Dy}_{0.6}\text{PO}_4$ showed an average fiber push-out stress of 30 MPa that was attributed to transformation plasticity and volume reduction

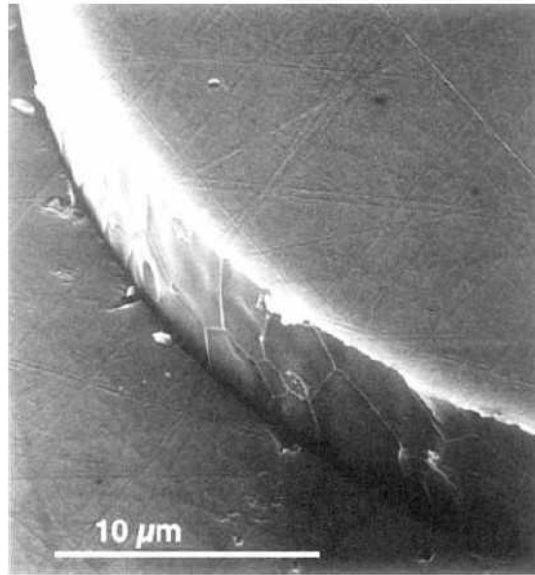


Figure 1.4: SEM image of monazite coated fiber after indentation push-out test [21].

during localized phase transformations [31]. Further investigation of the coating using transmission electron spectroscopy (TEM) discovered that portions of the damaged regions underwent phase transformations from xenotime to anhydrite structure (orthorhombic, Amm) and to monazite [32]. Transformation plasticity is the softening of a material due to the atomic rearrangement that occurs during phase transformation. When high enough shear stresses act on the coating, small regions undergo pressure-induced phase transformations. The increased plasticity during transformation and the volume reduction further promote fiber sliding within the matrix. These results suggest that the fiber push-out stress may be significantly influenced by the transformation pressure of the coating material.

1.3 Pressure-Induced Phase Transformations

REPO₄s have been studied under high pressure by Raman spectroscopy [33-39], X-ray and neutron diffraction [34, 37-44], and theoretical calculations [33, 38-40, 43-45]. Monazite LaPO₄ has been observed to undergo a phase transformation to a barite-type structure at 26 GPa while other monazites remained stable beyond 30 GPa [41, 46]. Xenotime REPO₄s undergo phase transformations at lower pressures. Experimental xenotime REPO₄ phase transformation pressure as a function of rare-earth ionic radius (eight-fold coordination [47]) are plotted in Figure 1.5 for xenotime-to-monazite transformations. An underlying trend of increased transformation pressure with decreasing rare-earth radius is shown. The xenotime REPO₄s with the smallest cation radii such as YbPO₄ and LuPO₄ were excluded since they transform directly to the scheelite (tetragonal, I4₁/a) phase at pressures of 22 GPa and 19 GPa, respectively [48]. The xenotime REPO₄ with the smallest cation radius presented in Figure 1.5 is TmPO₄ and it has been observed to transform to both the monazite and scheelite phases. The transformation pressures for TmPO₄ were measured at 20.3 GPa [34] and 21.2 GPa [39]. The adjacent xenotime REPO₄s with larger cations transformed at 18.8 GPa for HoPO₄ [39] and 17.3 GPa for ErPO₄ [41]. Yttrium has a similar cation radius and YPO₄ transforms to the monazite phase at 16.3 GPa [38] and 19.7 GPa [41]. It has been reported that DyPO₄ has a transformation pressure of ~ 13 GPa [34] but this has not been experimentally documented. Xenotime single-crystal TbPO₄ underwent a phase transformation to the monazite phase under high pressure observed by Raman spectroscopy (~9.5 GPa [35]) and X-ray diffraction (XRD) (9.8 - 10.1 GPa [40]). Solid-solution orthophosphates have effective rare-earth radii that can be approximated by linear interpolation between the two cation radii. For example, Tb_{0.5}Gd_{0.5}PO₄ has a cation effective rare-earth radius above that of TbPO₄ with a transformation pressure of 10.5 GPa to monazite [42].

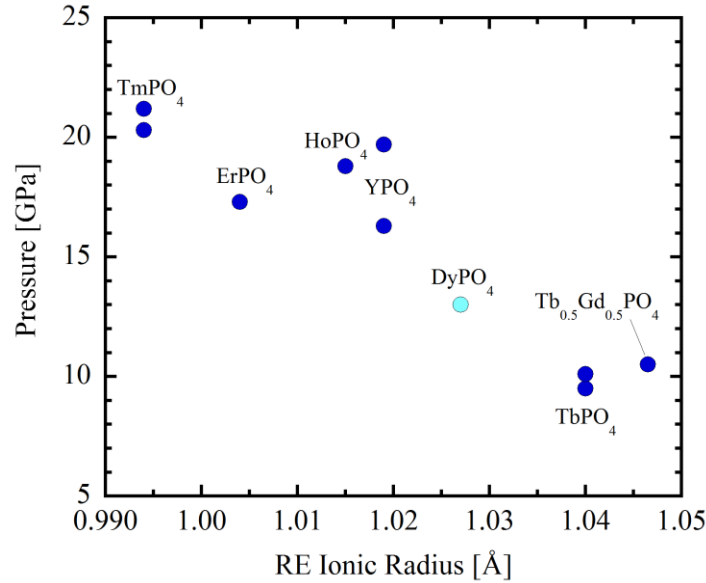


Figure 1.5: Compiled experimental phase transformation pressures of xenotime REPO₄ (RE ionic radii based on eight-fold coordination of the xenotime structure).

1.4 Research Overview

This thesis investigates the high-pressure behavior of REPO₄ compositions that have shown favorable reduction in fiber push-out stress, as well as relevant compositions for comparison. Gd_{0.4}Dy_{0.6}PO₄ was shown to have a lower fiber push-out stress than DyPO₄ which coincides with the solid solution having a larger effective rare-earth radius. Prior to this work, the transformation pressures of Gd/Dy solid solutions and pure DyPO₄ had not been experimentally documented. Raman scattering data was collected from polycrystalline powders at room temperature under incremental high pressures inside a DAC. The phase transformation pressure and line crossing of TbPO₄, DyPO₄ and Gd_xDy_(1-x)PO₄ (x = 0.4, 0.5, 0.6) were extracted and analyzed.

Chapter 2 details the experimental methods of this research. The procedure for synthesis is described along with technical data for the characterization of each sample. Verification of the

crystal structure was conducted using X-ray diffraction (XRD) with combined differential thermal analysis (DTA) and thermogravimetric analysis (TGA) for comparison. The powder morphology after synthesis was documented using scanning electron microscopy (SEM) and the compositions were verified using energy dispersive spectroscopy (EDS). The techniques for collecting high-pressure structural data for the materials through DAC experiments with *in situ* Raman spectroscopy are explained.

Chapter 3 presents a research paper to be submitted to the peer-reviewed Journal of Physics: Condensed Matter. This chapter details the analysis of the data and documents the results extracted from the experiments. A comparison to similar xenotime REPO₄s is made and the possible implications are discussed. Limitations of the pressure medium and pressure calibration using ruby fluorescence are addressed.

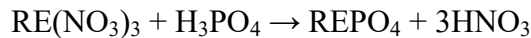
Chapter 4 concludes the thesis with a summary of this work and highlights the accomplishments of my research. The chapter is finalized with suggestions for future research to better understand the high-pressure behavior of these materials.

CHAPTER 2 EXPERIMENTAL METHODS

This chapter describes the synthesis, characterization, and high-pressure testing of TbPO₄, DyPO₄ and the Gd_xDy_(1-x)PO₄ (x = 0.4, 0.5, 0.6) solid solutions. The initial step of this project was to synthesize the rare-earth orthophosphate powders from nitrate precursors. The method mimics the synthesis process of the REPO₄ fiber coatings tested for fiber push-out stress by Hay *et al.* [49]. After synthesis, the powders were characterized with X-ray diffraction (XRD) to verify the structure along with differential thermal analysis (DTA) and thermogravimetric analysis (TGA) for comparison of the behavior during thermal processing. The powder morphology was documented using scanning electron microscopy (SEM) and the compositions of the materials were determined through energy dispersive spectroscopy (EDS). Finally the REPO₄s were tested in diamond anvil cell (DAC) experiments with *in situ* Raman spectroscopy and the spectra were analyzed.

2.1 Materials Synthesis

The materials were synthesized by aqueous precipitation using rare-earth nitrates and phosphoric acid as described by Boakye *et al.* [5], according to the reaction:



Reagent-grade gadolinium nitrate, dysprosium nitrate, and terbium nitrate (Alfa Aesar, Ward Hill, MA) were used without further modification. The rare-earth nitrates (RE(NO₃)₃) were dissolved in 200 mL of deionized water. Separately a 1:1 molar ratio of phosphoric acid

(H₃PO₄) to rare-earth nitrate was diluted with 200 mL of deionized water (0.1 mol RE(NO₃)₃ to 0.1 mol of 14.615 M H₃PO₄ or 6.842 mL). The two solutions were combined in a 500 mL beaker with a stir bar set to rotate at 400 rpm. Approximately 50 mL of ammonium hydroxide (NH₄OH) was added as needed to adjust from the initial pH of ~1 to ~10 in order to more rapidly precipitate particles. The pH was measured with a VWR sympHony SB70P pH meter (Radnor, PA). Solid solutions of Gd_xDy_(1-x)PO₄ were synthesized with x = 0.4, 0.5, 0.6. The particles were separated out of solution through filter paper (Grade 1 Whatman, 11 μm) and were dried in a fume hood for 48 hours. Remaining moisture was evaporated in a drying oven at 100°C as needed.

2.2 Phase Analysis and Thermal Behavior

This section describes the incremental heat treatments characterized by XRD and the thermal analysis using DTA/TGA. These methods were used to determine the structure of the synthesized powders and their behavior during thermal processing. The results are plotted and compared in 2.2.1 and 2.2.2., and the behavior in both techniques is discussed in 2.2.3.

2.2.1 X-Ray Diffraction (XRD)

The REPO₄s were characterized by powder diffraction using a PANalytical PW3040 X-ray Diffractometer (Almelo, Netherlands) to confirm xenotime crystal structure and phase purity after calcining. Powder diffraction files (PDFs) used for reference were DyPO₄ spectra 00-026-0593 (tetragonal) and 00-045-0041 (monoclinic). PDFs for TbPO₄ spectra were 00-032-1292 (tetragonal) and 00-046-1331 (monoclinic).

Crystal structure as a function of calcining temperature was measured in incremental heat treatments starting from 600 °C and increasing at 100 °C increments. TbPO₄ and DyPO₄ were characterized up to 1200 °C and the Gd_xDy_(1-x)PO₄ solid solutions up to 1400 °C. The samples were heated at a rate of 10 °C/min. and held at the maximum temperature for 1 hour. XRD was collected after each heat treatment. Figures 2.1 through 2.5 show plots of the XRD patterns at incremental temperatures for TbPO₄, DyPO₄, and the Gd_xDy_(1-x)PO₄ solid solutions. TbPO₄ and DyPO₄ show phase purity at 1200°C and were calcined at 1200°C for 2 hours before testing. The Gd_xDy_(1-x)PO₄ solid solutions show phase purity at 1400°C and were calcined at 1400°C for 2 hours prior to testing.

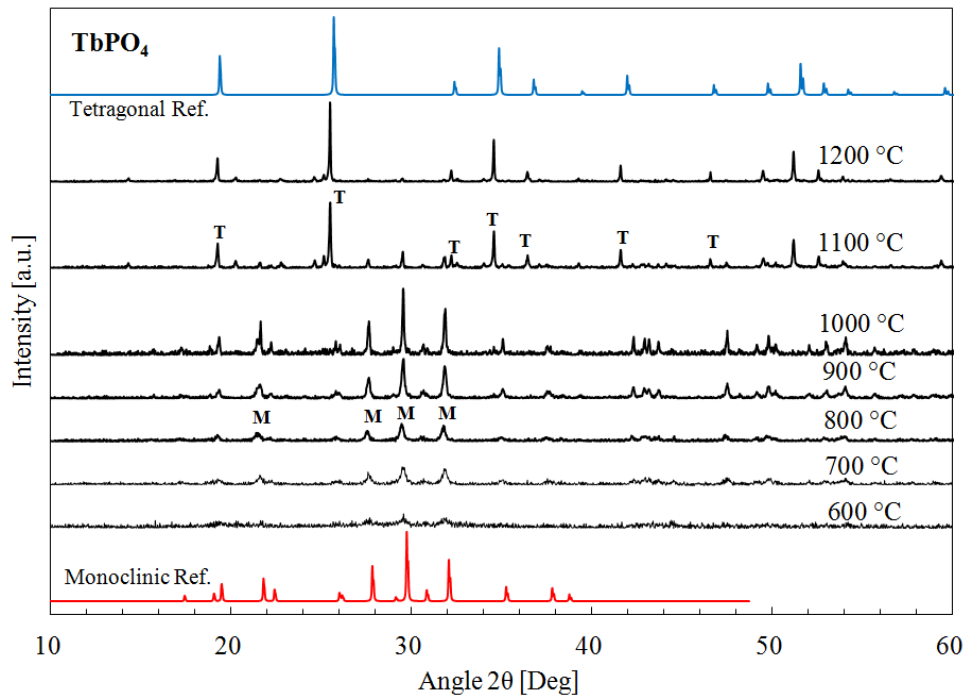


Figure 2.1: TbPO₄ XRD Incremental Heat Treatments

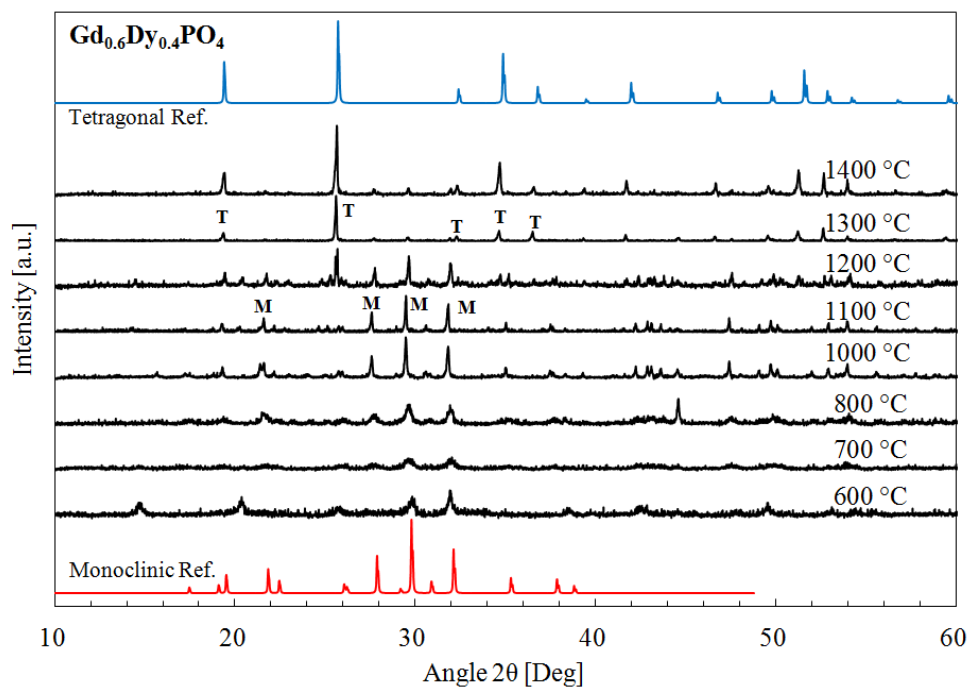


Figure 2.2: $Gd_{0.6}Dy_{0.4}PO_4$ XRD Incremental Heat Treatments

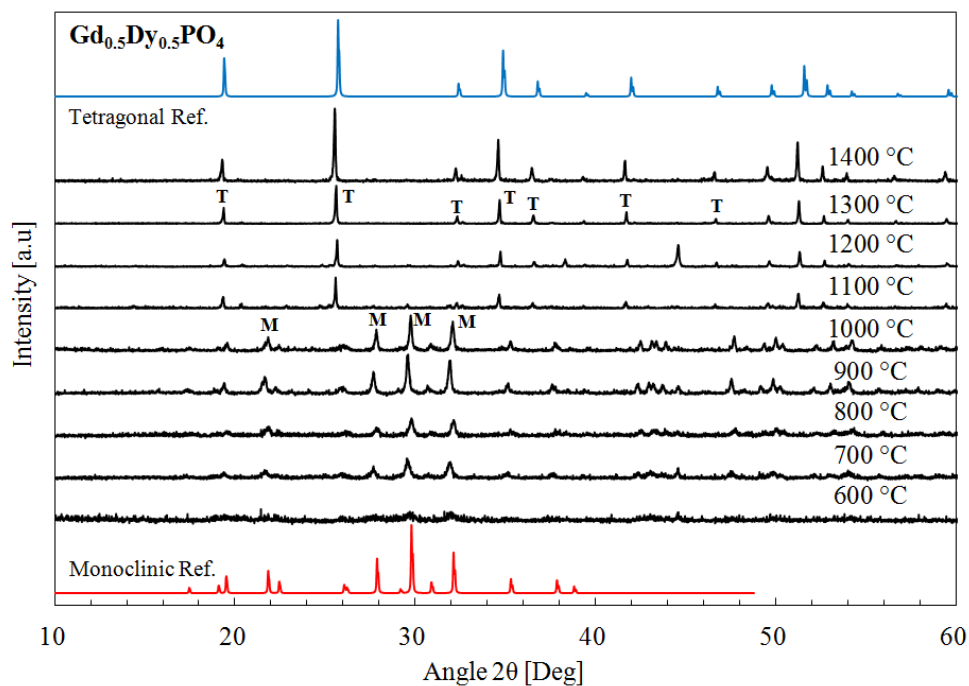


Figure 2.3: $Gd_{0.5}Dy_{0.5}PO_4$ XRD Incremental Heat Treatments

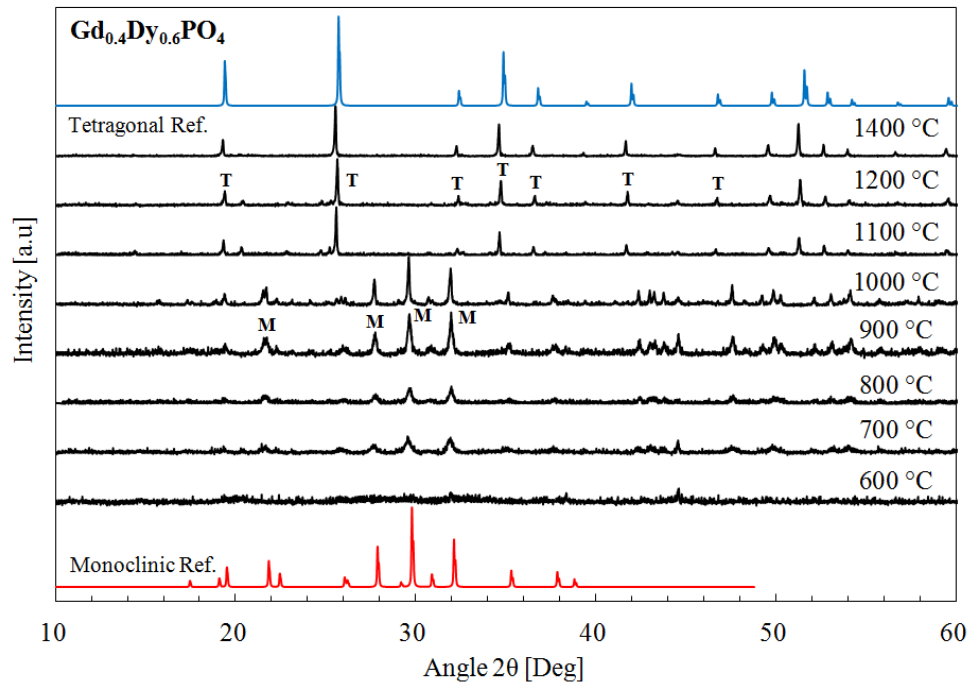


Figure 2.4: Gd_{0.4}Dy_{0.6}PO₄ XRD Incremental Heat Treatments

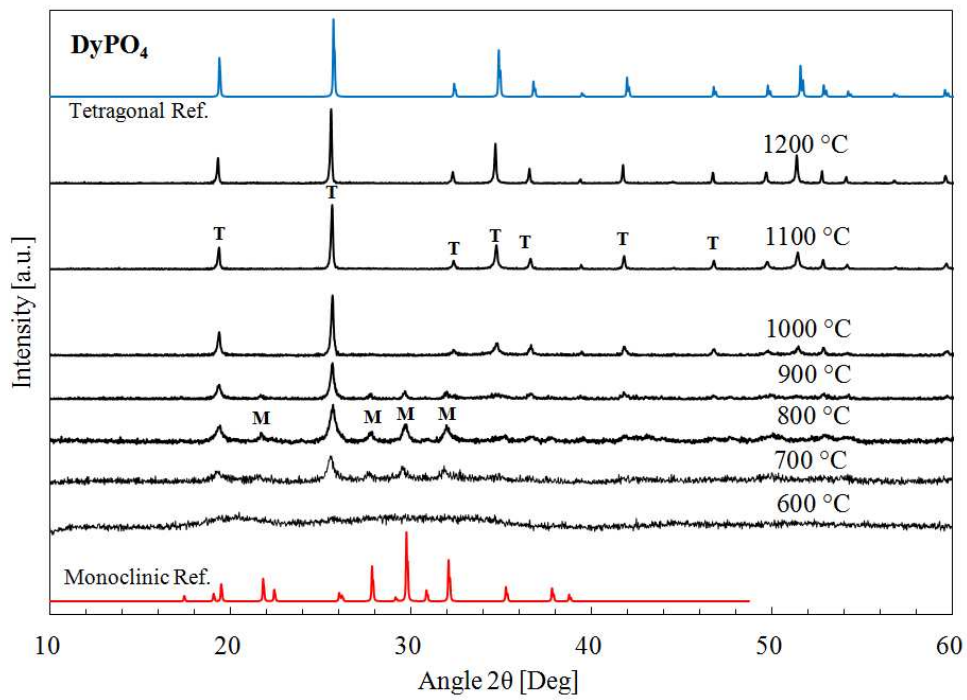


Figure 2.5: DyPO₄ XRD Incremental Heat Treatments

2.2.2 Differential Thermal Analysis (DTA)/Thermogravimetric Analysis (TGA)

As precipitated amorphous powders were analyzed using a Setram SETSYS Evolution TGA/DTA (Caluire-et-Cuire, France). All samples were heated up to 1200 °C at a rate of 10 °C/min. Figures 2.6 through 2.10 show plots of the DTA and TGA data during heating for TbPO₄, DyPO₄, and the Gd_xDy_(1-x)PO₄ solid solutions. At temperatures below 400 °C, the mass loss and heat fluxuations can be attributed to the evaporation of water moisture and other possible contaminants in the powders, such as ethanol from processing. All samples produce an exotherm around 750 °C. There is no corresponding mass loss in this temperature range, thus the exotherm is attributed to a first-order phase transformation, correlating to the crystallization of the amorphous powders.

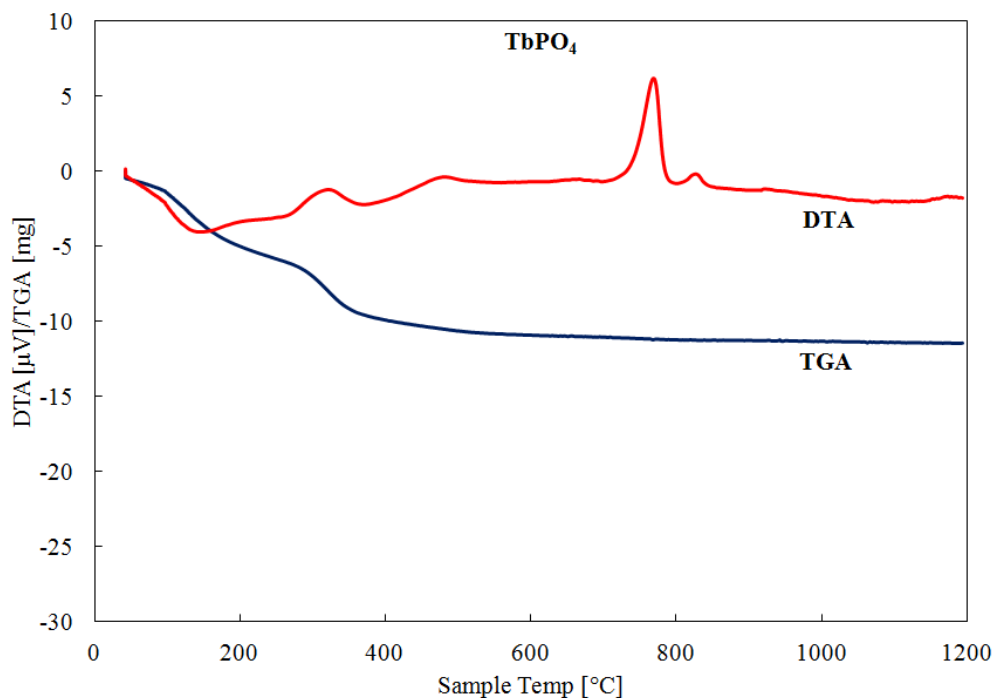


Figure 2.6: DTA/TGA data of TbPO₄ after synthesis

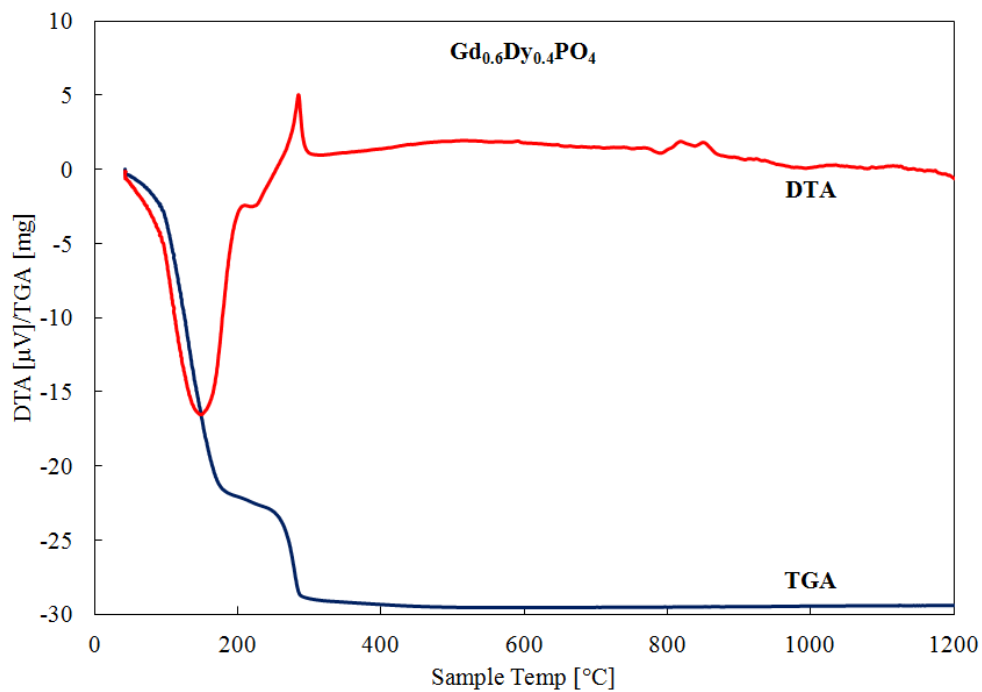


Figure 2.7: DTA/TGA data of Gd_{0.6}Dy_{0.4}PO₄ after synthesis

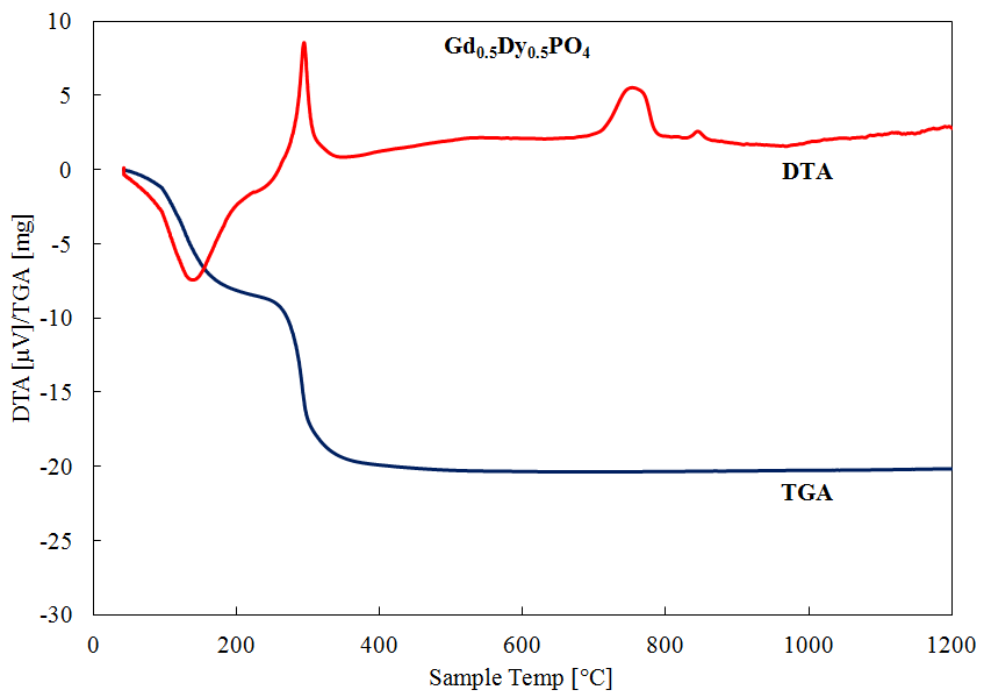


Figure 2.8: DTA/TGA data of Gd_{0.5}Dy_{0.5}PO₄ after synthesis

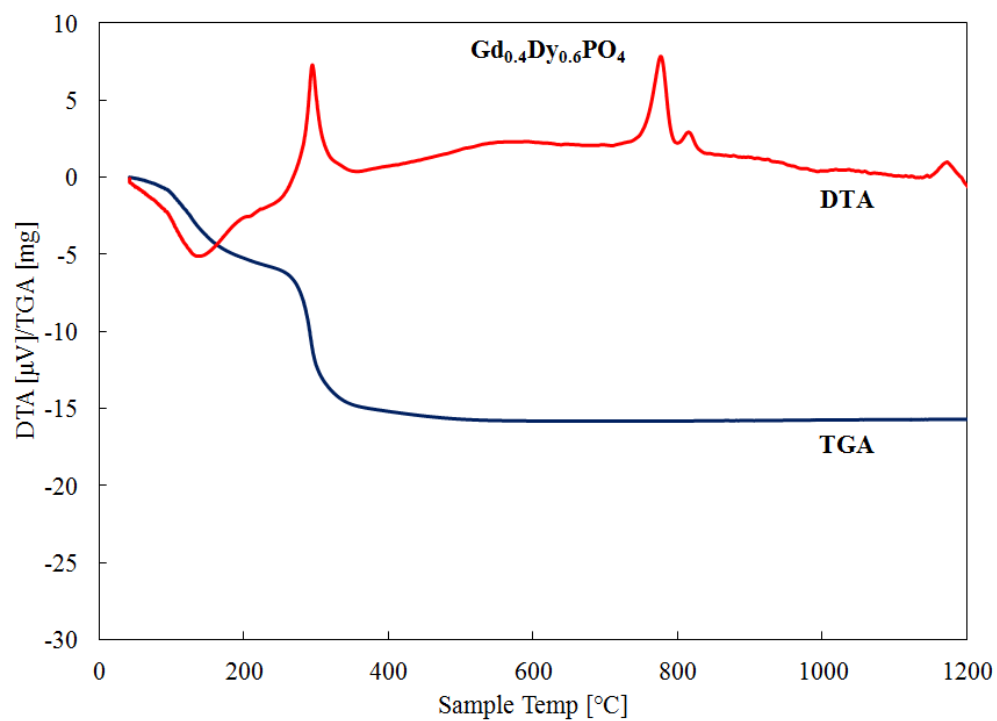


Figure 2.9: DTA/TGA data of $Gd_{0.4}Dy_{0.6}PO_4$ after synthesis

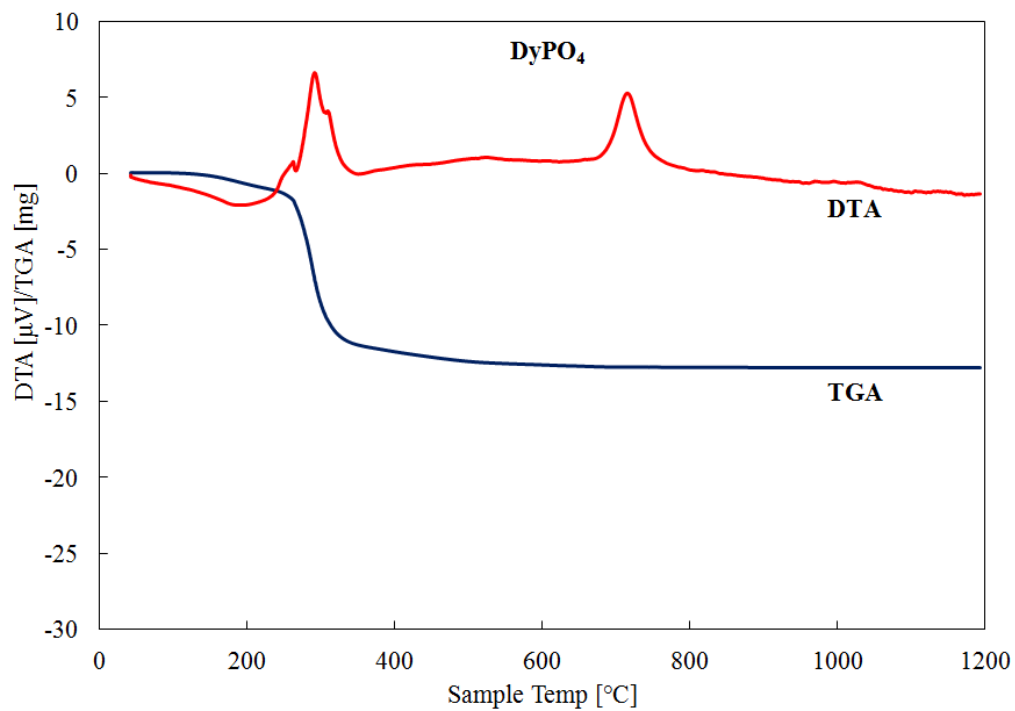


Figure 2.10: DTA/TGA data of $DyPO_4$ after synthesis

2.2.3 Thermal Behavior Comparison

Crystallization of the amorphous powders to the monazite phase during incremental heat treatments observed by XRD begins at 700°C. DTA of the powders identified an exotherm associated with crystallization between 750-800°C. These results are sufficiently repeatable between the different samples. The lower crystallization temperature in the XRD process can be explained by the difference between the processing steps of the two methods. DTA increases the temperature at a constant rate and doesn't include any time segments with constant temperature. The XRD heat treatments are a series of individual processes with the same loading rate but include a 1 hour constant temperature segment. So the XRD data includes more cumulative hours of annealing time than the DTA process which results in the crystallization occurring at a lower temperature in the XRD method.

2.3 Scanning Electron Microscopy (SEM)/Energy Dispersive X-Ray Spectroscopy(EDS)

SEM images of the powder samples were collected after synthesis. The images were collected using an FEI Quanta 600E SEM (Hillsboro, OR) with a tungsten filament. Figures 2.11 through 2.15 show SEM images of TbPO₄, DyPO₄, and the Gd_xDy_(1-x)PO₄ solid solutions after synthesis. The materials are amorphous after precipitation and form micro-scale agglomerates of nano-scale particles.

Sample compositions were measured using an EDAX Inc. EDS (Mahwah, NJ) during the SEM imaging. Three different regions were measured for gadolinium and dysprosium content to calculate Gd/Dy ratios. The results are shown in Table 2.1. The ratios were within reasonable error with only the Gd_{0.5}Dy_{0.5}PO₄ ratio deviating slightly.

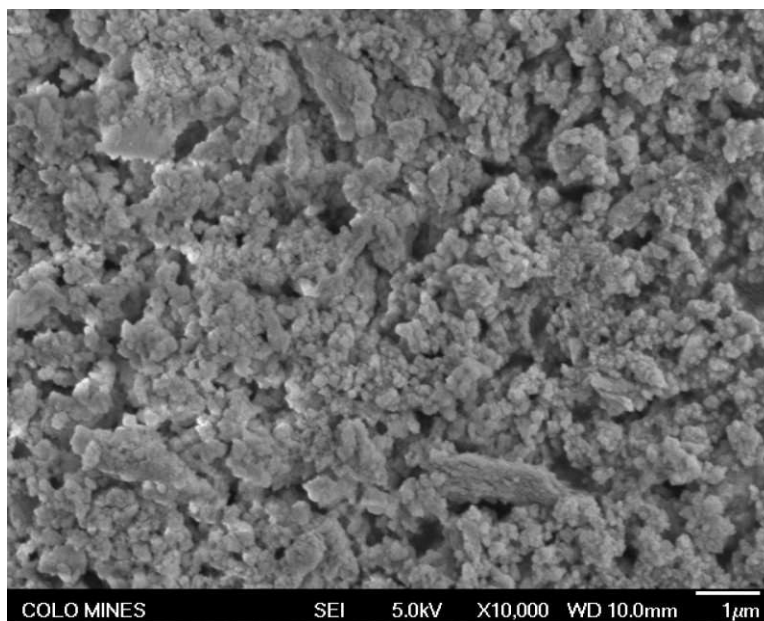


Figure 2.11: SEM image of TbPO₄ as precipitated

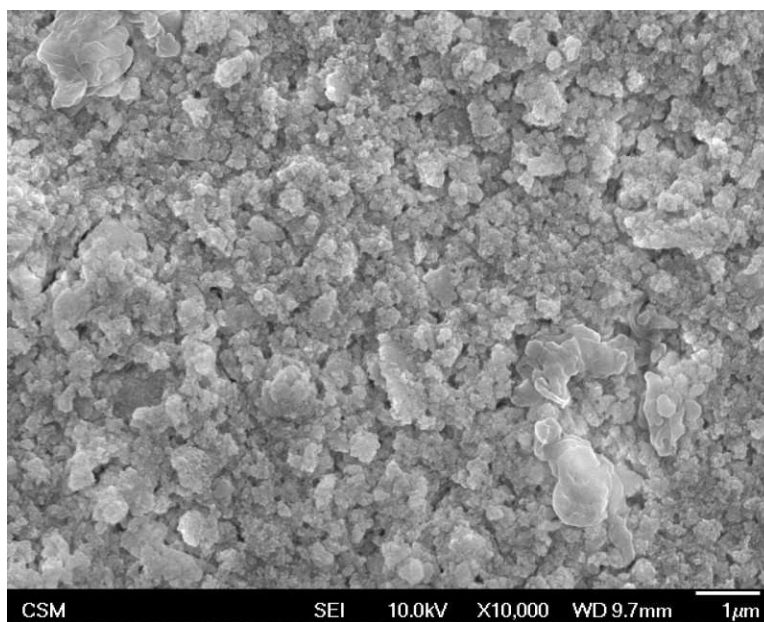


Figure 2.12: SEM image of Gd_{0.6}Dy_{0.4}PO₄ as precipitated

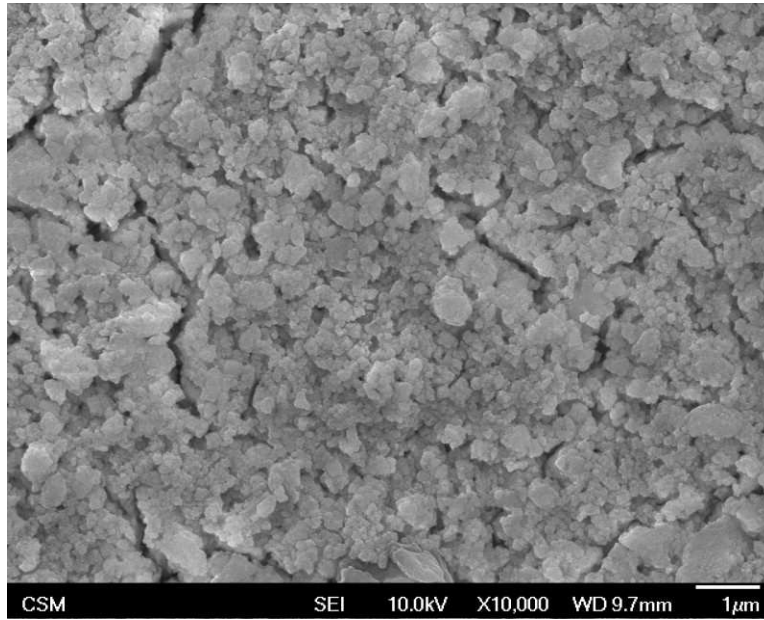


Figure 2.13: SEM image of Gd_{0.5}Dy_{0.5}PO₄ as precipitated

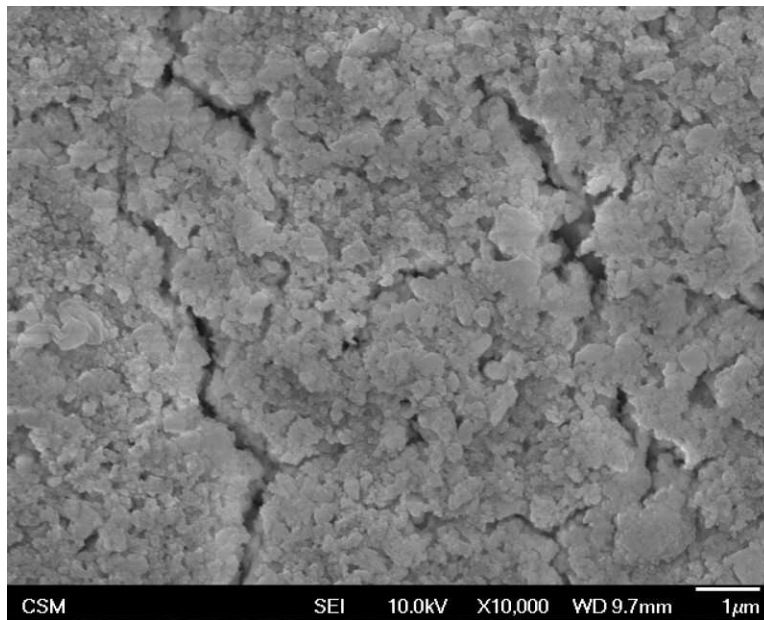


Figure 2.14: SEM image of Gd_{0.4}Dy_{0.6}PO₄ as precipitated

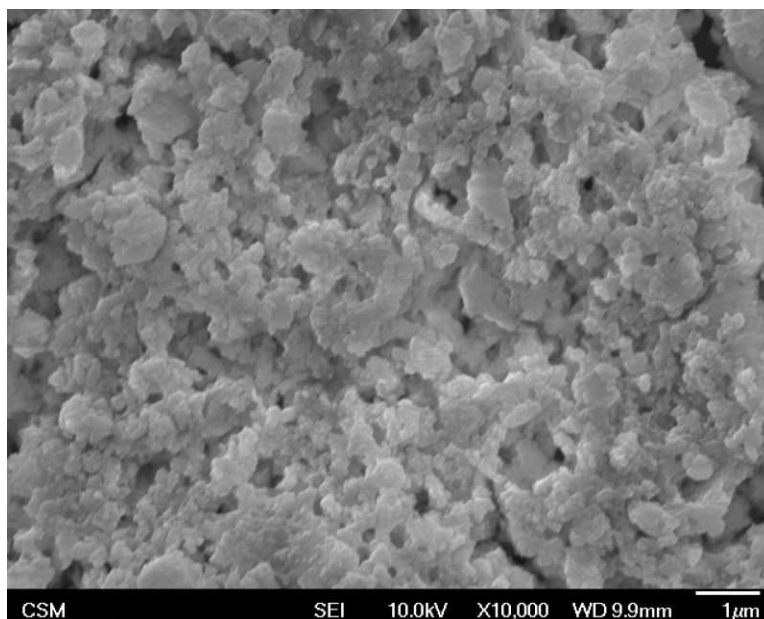


Figure 2.15: SEM image of DyPO₄ as precipitated

Table 2.1: RE ratios in solid solutions measured by EDS.

Gd_{0.6}Dy_{0.4}PO₄	Average	Ideal
Gd to RE ratio by At%	0.60	0.6
Dy to RE ratio by At%	0.40	0.4
Gd_{0.5}Dy_{0.5}PO₄		
Gd to RE ratio by At%	0.52	0.5
Dy to RE ratio by At%	0.48	0.5
Gd_{0.4}Dy_{0.6}PO₄		
Gd to RE ratio by At%	0.40	0.4
Dy to RE ratio by At%	0.60	0.6

2.4 Diamond Anvil Cell (DAC) with *in situ* Raman Spectroscopy

High-pressure data were collected through DAC experiments. Samples are compressed in between two diamond culet faces contained within a 301 stainless steel gasket. The chamber is filled with a pressure medium in order to achieve hydrostatic stress conditions. The diamonds are chosen to have low birefringence and low fluorescence which is necessary for *in situ*

spectroscopy. Electromagnetic radiation can be focused through the diamonds onto the sample and either the reflected or transmitted spectrum can be collected. XRD is one common method for measuring structural parameters. But due to the small sample size (~50 μm diameter) a large flux is necessary to generate a relevant diffraction pattern which requires the use of synchrotron radiation. Alternatively, Raman spectroscopy is a more readily available method and was implemented in this project. Specifications of the DAC, pressure medium, and techniques are described in further detail in Chapter 3.

Raman spectroscopy measures the changes in wavelength of light due to interactions between photons and lattice vibrations in the material's structure. This provides a unique thumbprint of a material and allows for identification of changes in the structure. Monochromatic light is focused on the sample and the scattered light is collected. The change in wavelength between the incident light and the reemitted light is due to a loss or gain in energy through a scattering event with the material. The emission of a photon with a lower energy is called Stokes scattering where a higher energy is called anti-Stokes. This project uses Stokes scattering data which is more commonly used. Specifications of the Raman spectrometer are described further in Chapter 3.

Previous studies on some xenotime REPO_4 phase transformations have identified an intermediate anhydrite phase between the transformation from xenotime to monazite using XRD [31, 32, 42]; however, other studies using Raman spectroscopy have not noted the presence of the anhydrite phase. Further investigation shows that the Raman modes of the anhydrite phase are very similar to the xenotime phase making the distinction difficult to observe. Figure 2.16 shows the Raman spectra of anhydrite and xenotime side by side for comparison. The REPO_4 anhydrite Raman spectrum is not available so the reference used is for anhydrite CaSO_4 from the

RRUFF mineral spectra database, ID: R040061.3. Exact peak locations are expected to differ, but the number and relative intensities are expected to be comparable.

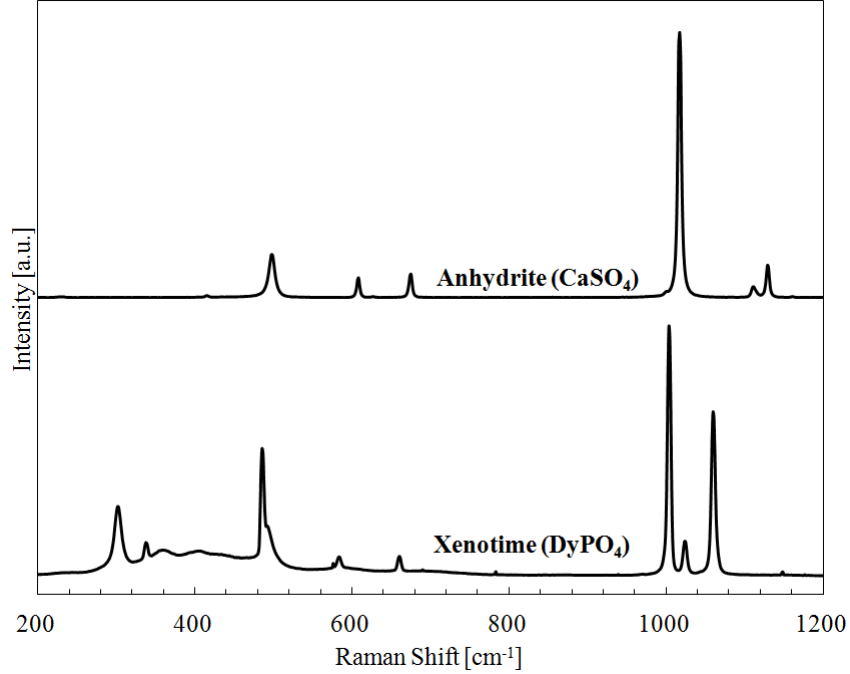


Figure 2.16: Raman spectra of anhydrite (CaSO_4) and xenotime (DyPO_4)

Pressure measurements within the DAC chamber were calculated using the ruby fluorescence method. A small piece of ruby is placed inside the chamber with the sample and pressure medium. Ruby emits two strong fluorescent peaks (R_1 and R_2 emission lines) during Raman spectroscopy, both of which can be used to calculate pressure. Used in this study, the R_1 line has a larger intensity and is more common in pressure measurements. The calibration was reported by Mao *et al.* [50] and later refined by Zha *et al.* [51], which is shown in Equation 2.1.

$$P = \frac{A}{B} \left[\left(\frac{\lambda}{\lambda_0} \right)^B - 1 \right] \quad (2.1)$$

The calculated pressure is a function of the R line at atmospheric pressure (λ_0) and the high-pressure R line (λ). The initial slope is fixed at a constant $A=1904$ GPa. A non-linear least squares fit of calibrated high-pressure MgO data gives $B=7.715$ (for hydrostatic conditions). Figure 2.17 displays an example REPO₄ Raman spectrum and the ruby fluorescent R lines. There is no overlap in ruby and REPO₄ spectra to complicate data analysis.

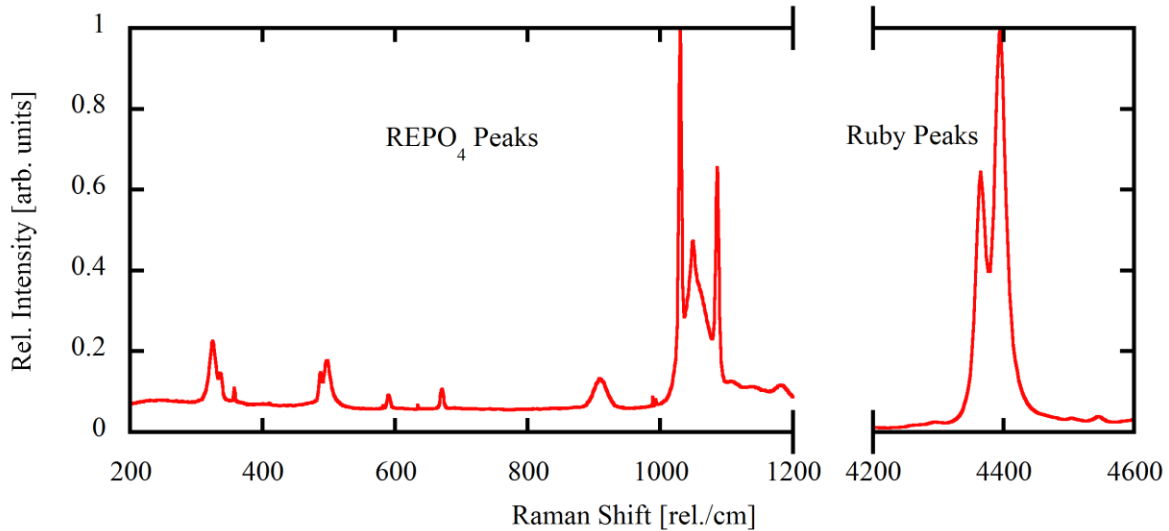


Figure 2.17: Raman spectra of xenotime (DyPO₄) and ruby fluorescence at atmospheric pressure

2.5 Data Analysis

The Raman spectroscopy data were analyzed using a customized Mathematica code. Lorentzian functions were fitted to the modes to identify peak locations, a common distribution used to match spectral broadening. Due to the complexity of the REPO₄ spectra and the large number of peaks, the Raman modes were partitioned into five groups before applying a Lorentzian fit. The initial step of the program imported and normalized the ruby and the REPO₄ spectra. The R₁ peak location is extracted from the Lorentzian peak fit and the used to calculate the pressure [51]. Plots of the spectra, the peak fits, and the peak locations were generated to visually confirm the analysis. Similar steps were taken for the partitioned REPO₄ spectra. An

example of a Lorentzian fit on a partition of a DyPO₄ spectrum is shown in Figure 2.18. The peak locations overlaid on the full Raman spectrum are shown in Figure 2.19. The peaks were then exported and reviewed with the corresponding pressure measurement for further analysis of the high pressure behavior and transformation pressure.

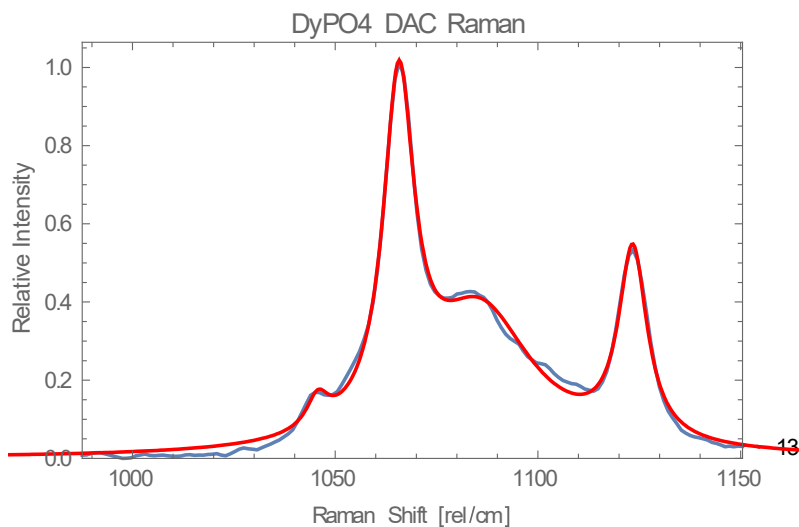


Figure 2.18: Lorentzian function (red) fit to a DyPO₄ Raman spectrum (blue).

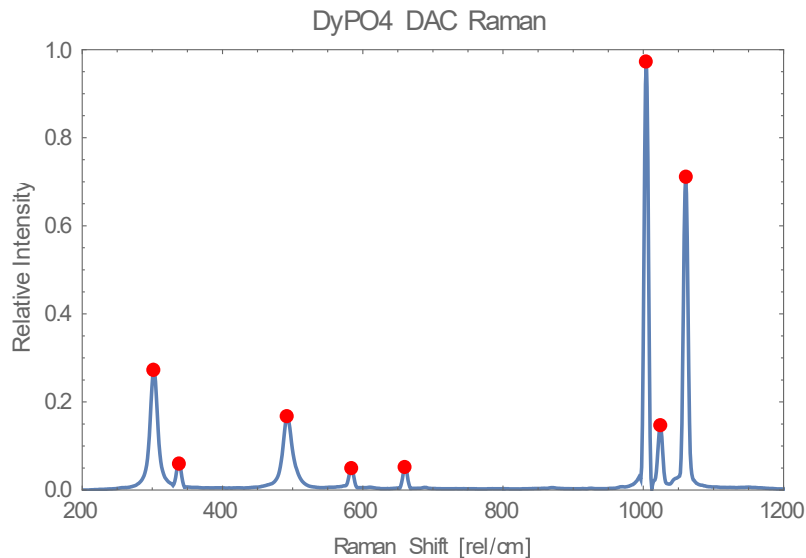


Figure 2.19: Peak locations from Lorentzian analysis (red) overlaid with the DyPO₄ Raman spectrum (blue).

CHAPTER 3 RESEARCH PAPER: *IN-SITU* RAMAN SPECTROSCOPY OF PRESSURE-INDUCED PHASE TRANSFORMATIONS IN DyPO_4 AND $\text{Gd}_x\text{Dy}_{(1-x)}\text{PO}_4$

The chapter contains the manuscript titled “In-situ Raman spectroscopy of pressure-induced phase transformations in DyPO_4 and $\text{Gd}_x\text{Dy}_{(1-x)}\text{PO}_4$.” The research paper was co-authored by Taylor M. Wilkinson (Colorado School of Mines, Golden, CO), Dr. Bianca Haberl (Oak Ridge National Laboratory), and Dr. Corinne Packard (Colorado School of Mines, Golden, CO). This chapter details the analysis of the data and documents the results extracted from the experiments. A comparison to similar xenotime REPO_4 s is made and the possible implications are discussed. Limitations of the pressure medium and pressure calibration using ruby fluorescence are addressed.

3.1 Manuscript – Abstract

Xenotime DyPO_4 and $\text{Gd}_x\text{Dy}_{(1-x)}\text{PO}_4$ ($x = 0.4, 0.5, 0.6$) (tetragonal $I4_1/amd$ zircon structure) have been studied at ambient temperature under high pressures inside a diamond anvil cell with *in situ* Raman spectroscopy. The typical Raman-active modes of the xenotime structure were observed at low pressures and the appearance of new Raman peaks at higher pressures indicated a phase transformation to a lower symmetry structure – likely monoclinic. Raman mode softening was observed, resulting in a line crossing at approximately 7-8 GPa for each material and preceding the phase transformation. The onset of phase transformation for DyPO_4 occurred at a pressure of 15.3 GPa. DyPO_4 underwent a reversible phase transformation and returned to the xenotime phase after decompression. The transformation pressures of the solid solutions ($\text{Gd}_x\text{Dy}_{(1-x)}\text{PO}_4$) were in the range of 10 – 12 GPa. The $\text{Gd}_x\text{Dy}_{(1-x)}\text{PO}_4$ solid solutions yielded partially reversible phase transformations, retaining some of the high-pressure phase spectrum while reforming xenotime peaks during decompression. The substitution of Gd into

DyPO₄ decreased the transformation pressure relative to pure DyPO₄. The ability to modify the phase transformation pressures of xenotime rare-earth orthophosphates by chemical variations of solid solutions may provide additional methods to improve the performance of specialized ceramic matrix composites.

3.2 Manuscript – Introduction

Rare-earth orthophosphates (REPO₄s) are non-oxidizing, chemically stable ceramics that plastically deform easily compared to other oxides with similar melting temperatures. They have shown potential as fiber coatings in oxide-oxide ceramic matrix composites (CMCs). CMC fiber coatings initiate crack deflections along the weakly bonded interface between the coating and fiber/matrix as well as facilitate fiber sliding within the matrix [16-20, 52]. Certain REPO₄ fiber coatings with the xenotime structure (tetragonal, I4₁/amd) have demonstrated a reduction in fiber push-out stress compared to other xenotime- and monazite-structured (monoclinic, P2₁/n) REPO₄ fiber coatings. Specifically Gd_{0.4}Dy_{0.6}PO₄ fiber coatings demonstrated significantly lower fiber push-out stresses than DyPO₄ and LaPO₄ fiber coatings [31]. Hay *et al.* partially attributed this behavior to transformation plasticity and volume reduction during localized phase transformations from xenotime to monazite. If the fiber coating can phase transform at a lower pressure, it could plastically deform more easily at lower stresses, suggesting that the fiber push-out stress may be significantly influenced by the transformation pressure of the coating material.

Anhydrous REPO₄s crystallize into either the xenotime structure (tetragonal, I4₁/amd) or the monazite structure (monoclinic, P2₁/n) depending principally on the rare-earth (RE) radius. Orthophosphates with heavy, smaller REs (Tb to Lu) are more thermodynamically stable in the xenotime structure while orthophosphates with light, larger REs (La to Gd) are most stable in the monazite structure at ambient temperature and pressure [1, 2]. Xenotime has ~5% larger molar

volume than monazite [3, 4]. Materials near the monazite-xenotime boundary (between Gd and Tb) have been observed to crystallize into either phase or a combination of both phases, depending on the specific processing conditions. DyPO₄ and TbPO₄ both take on a metastable monazite phase at lower calcining temperatures (~700 °C) which then transform to xenotime at elevated temperatures [5]. Similarly, TbPO₄ exhibits a room temperature phase transformation from xenotime to the monazite phase under pressure [35, 40].

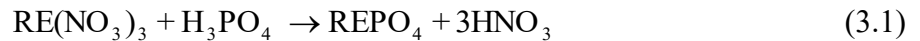
Characterization of the high-pressure REPO₄ phases is important for engineering applications as well as understanding more about historical geological conditions during the formation of the Earth's crust [53]. REPO₄s have been studied under high pressure by Raman spectroscopy [33-39], X-ray and neutron diffraction [34, 37-44], and theoretical calculations [33, 38-40, 43-45]. Phase transformations are reported for all elemental lanthanide xenotimes from Tb to Tm, with the exception of Dy, from diamond anvil cell (DAC) experiments. A review of these transformation pressures reveals an underlying trend of increased transformation pressure with decreasing rare-earth radius [47]. The xenotime REPO₄ with the smallest cation used for comparison is TmPO₄ and it has been observed to transform to both the monazite and scheelite phases. Through X-ray diffraction (XRD) the transformation pressure for TmPO₄ was measured at 20.3 GPa [34] and 21.2 GPa [39] in two separate studies. Adjacent xenotime REPO₄s with larger cations transformed at 17.3 GPa for ErPO₄ [41] and 18.8 GPa for HoPO₄ [39] – all measured by XRD. Yttrium has a slightly larger cation radius than holmium and YPO₄ transforms to the monazite phase at similar pressures (16.3 GPa [38] and 19.7 GPa [41] are reported). Xenotime TbPO₄ transforms to the monazite phase under high pressure observed by Raman spectroscopy (~9.5 GPa [35]) and XRD (9.8 - 10.1 GPa [40]). It has been reported that DyPO₄ has a higher transformation pressure than TbPO₄ (~ 13 GPa) [34] but the spectra have not

been experimentally documented in the open literature. The high-pressure behavior of the xenotime REPO₄ solid solution Tb_{0.5}Gd_{0.5}PO₄ has been documented as well. Solid-solution orthophosphates have effective rare-earth radii that can be approximated by linear interpolation between the two cation radii. Tb_{0.5}Gd_{0.5}PO₄ has a cation effective rare-earth radius above that of TbPO₄ but it has a similar monazite transformation pressure of 10.5 GPa [42]. In non-hydrostatic testing, the REPO₄ solid solution Gd_{0.4}Dy_{0.6}PO₄ was shown to have a lower fiber push-out stress than DyPO₄, which also coincides with the solid solution having a larger effective rare-earth radius [31]. But the hydrostatic transformation behavior and pressures of Gd_xDy_(1-x)PO₄ solid solutions and pure DyPO₄ have not been experimentally documented. This information could provide additional insight into the performance of these REPO₄ fiber coatings.

In this paper, we characterize the phase transformation pressure and evaluate the reversibility of the transition of xenotime REPO₄s that have shown favorable reduction in fiber push-out stress. Raman scattering data are reported from polycrystalline DyPO₄, TbPO₄, and Gd_xDy_(1-x)PO₄ (x = 0.4, 0.5, 0.6) powders at room temperature under incremental high pressures inside a DAC, from which phase transformation is characterized. The transformation pressures and behavior have been compared to those of other lanthanide xenotimes.

3.3 Manuscript – Experimental Methods

The materials were synthesized by aqueous precipitation using rare-earth nitrates and phosphoric acid [5], according to the reaction in Equation 3.1.



Reagent-grade gadolinium nitrate, dysprosium nitrate, and terbium nitrate (Alfa Aesar, Ward Hill, MA) were used without further modification. The rare-earth nitrates were dissolved in deionized water and separately, a 1:1 molar ratio of phosphoric acid to rare-earth nitrate was

diluted with deionized water. The two solutions were combined and ammonium hydroxide was added as needed to adjust from the initial pH of ~ 1 to ~ 10 in order to more rapidly precipitate particles [5]. Solid solutions of $\text{Gd}_x\text{Dy}_{(1-x)}\text{PO}_4$ were synthesized with $x = 0.4, 0.5, 0.6$. TbPO_4 and DyPO_4 powders were calcined at 1200°C for 2 hours. Solid solution orthophosphates were calcined at 1400°C for 2 hours. Powder diffraction using a PANalytical PW3040 X-ray Diffractometer (Almelo, Netherlands) confirmed xenotime crystal structure and phase purity after calcining. Powder diffraction files (PDFs) 00-026-0593 (tetragonal) and 00-045-0041 (monoclinic) for DyPO_4 were used as reference spectra.

Samples were compressed by DAC in an Almax easyLab plateDAC (Almax easyLab Inc., Cambridge, MA) with a diamond culet size of $330\ \mu\text{m}$. Gaskets were fabricated from $250\ \mu\text{m}$ -thick 301 stainless sheet steel, indented to approximately $100\ \mu\text{m}$ thick with $250\ \mu\text{m}$ diameter holes at the center drilled by micro-EDM (electrical discharge machining). Raman spectra were collected *in-situ* through the diamond culets using a $532\ \text{nm}$ excitation laser on a WITek alpha300 spectrometer (WITek Instruments Corp. Knoxville, TN). A small quantity of ruby powder was sealed in the DAC with each sample for use as a pressure indicator. A 16:3:1 (by volume) solution of ethanol:methanol:water was used as the pressure medium and a 15 minute settle time was allowed after each increase in pressure. This medium has been shown to remain hydrostatic up to $\sim 10\ \text{GPa}$, becoming non-hydrostatic and introducing deviatoric stresses and pressure gradients at higher pressures [54], resulting in increases in the standard deviation of measurements across the sample chamber. In order to minimize error in pressure measurement, the sample Raman spectra and ruby Raman spectra were collected from the same location within the cell.

Raman data were processed in the WITek Project software with background subtraction and cosmic ray removal. A Savitsky-Golay filter was applied to increase the signal to noise ratio. Raman peak locations were determined by fitting Lorentzian peaks to the spectra. The ruby fluorescence method was used to calibrate pressure for each spectrum [50, 51]. The REPO₄ Raman peaks of interest are located between 200 and 1200 cm⁻¹ and the ruby fluorescence peak is found at ~4400 cm⁻¹, so there is no overlap between the Raman spectra of the pressure marker and REPO₄s.

3.4 Manuscript – Results and Discussion

Figure 3.1 shows selected Raman spectra of each material during compression in DAC experiments. The figure includes TbPO₄ (a) as the reference spectra, the solid solutions Gd_{0.6}Dy_{0.4}PO₄ (b), Gd_{0.5}Dy_{0.5}PO₄ (c), Gd_{0.4}Dy_{0.6}PO₄ (d), and lastly DyPO₄ (e). Raman spectra below 200 cm⁻¹ were not included in this study due to limitations of the Raman spectrometer. The Raman spectra between 750 and 950 cm⁻¹ have been excluded from the plots for emphasis of the relevant peaks. The spectra below 750 cm⁻¹ have been scaled up relative to the spectra above 950 cm⁻¹ for clarity. The initial Raman peaks and relative intensities of polycrystalline xenotime TbPO₄ are consistent with the results reported by Tatsi, *et al.* [35] for single-crystal TbPO₄. Xenotime DyPO₄ also matched the Raman spectra reported by Kontos, *et al.* [36]. The Raman shift wavenumbers for TbPO₄ and DyPO₄ are slightly higher in this study by comparison but the relative locations of peaks to one another are identical. The eight Raman modes and relative intensities previously reported for all other xenotime REPO₄s were observed in the initial Raman spectra of the Gd_xDy_(1-x)PO₄ solid solutions [1, 2, 33, 35, 36]. The observed ambient mode frequencies (ω_0) from this study are shown in Table 3.1 and are compared to the xenotime TbPO₄ results and mode assignments reported by Tatsi, *et al.* for reference [35].

During compression, changes in the Raman spectra include shifting of the peaks as the lattice is distorted under high pressure. Significant changes in the Raman spectra such as the appearance of new Raman peaks and loss of previously observed ones are an indication of phase transformation. The new peaks corresponding to a phase transformation are identified with an asterisk above the onset transformation spectrum in Figure 3.1. The increased quantity of Raman peaks at high pressure is characteristic of a lower symmetry phase. Several of the most obvious new peaks are marked with asterisks on the spectra, identifying the onset of phase transformation. The thermodynamically stable high-pressure phase of TbPO₄, HoPO₄, YPO₄, and ErPO₄ has been determined to be monazite through *ab initio* calculations and synchrotron XRD [39-41]. A previous high-pressure study of DyPO₄ went up to 7.6 GPa [36], which was not high enough to induce phase transformation and so the high-pressure phase was not observed. In this work, the high-pressure phases of DyPO₄ and the Gd_xDy_(1-x)PO₄ solid solutions have Raman peaks consistent with the monazite phase [35, 40]. The formation of the A_g (~1033 cm⁻¹) monazite mode that coincides with the elimination of the A_{1g} (~995 cm⁻¹) xenotime mode is the strongest indication of this transformation. In addition, the common emergence of peaks at ~290 cm⁻¹, ~455 cm⁻¹, ~480 cm⁻¹, and ~560 cm⁻¹ agrees with prominent monazite modes observed under high-pressure Raman spectroscopy [33, 35, 40]. Further characterization using XRD is necessary to definitively confirm the high-pressure phase of DyPO₄ and the Gd_xDy_(1-x)PO₄ solid solutions.

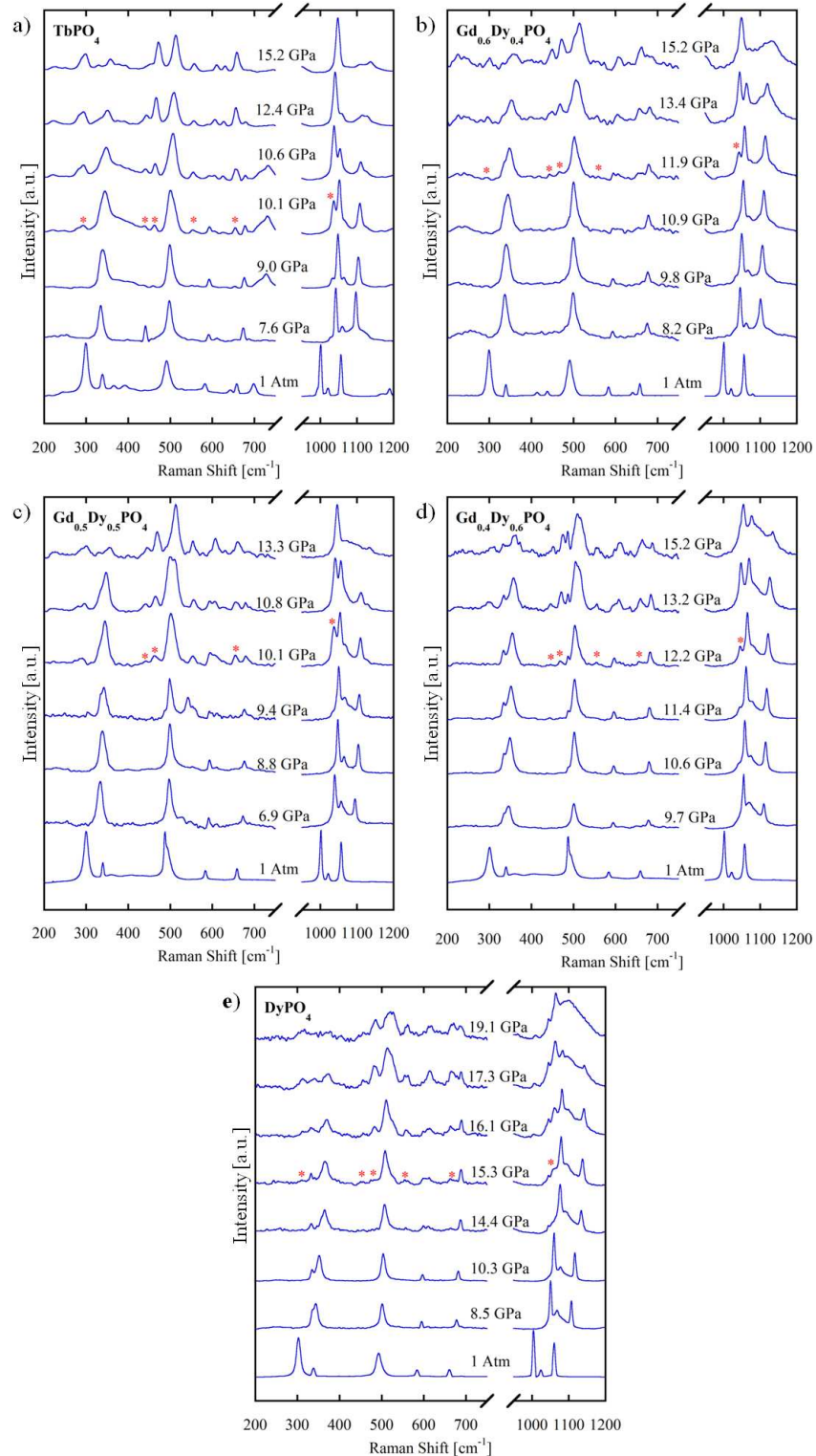


Figure 3.1: Selected Raman spectra of TbPO_4 (a), $\text{Gd}_{0.6}\text{Dy}_{0.4}\text{PO}_4$ (b), $\text{Gd}_{0.5}\text{Dy}_{0.5}\text{PO}_4$ (c), $\text{Gd}_{0.4}\text{Dy}_{0.6}\text{PO}_4$ (d), and DyPO_4 (e) during compression. Peaks associated with the onset of the phase transformation are indicated by *.

Analysis of the changes in Raman peak locations during compression provides additional insight to the effects of pressure on the Raman modes. Figure 3.2 shows the Raman peaks as a function of pressure for all spectra collected, including spectra omitted from Figure 3.1. Peaks associated with the initial xenotime phase are shown as black data points and the new peaks of the high-pressure phase are shown as red data points. The new peaks are distinct in that they lie outside the linear regression of the existing modes during compression and their relative intensities grew larger with subsequent pressure increases. Figure 3.2 (e) extends to 20 GPa in order to capture the higher-pressure transformation behavior of DyPO₄. The changes in Raman mode frequencies (ω) with increasing pressure (P) were monitored throughout testing and the slope of the linear fit $(\delta\omega/\delta P)_T$, was obtained for each mode. The slopes are shown in Table 3.1 alongside the TbPO₄ results obtained by Tatsi, *et al.* [35] and are observed to be similar.

Previous high-pressure Raman studies of REPO₄s have identified a line level crossing that precedes the subsequent phase transformation at higher pressures, which is a result of mode softening. TbPO₄ and DyPO₄ have both shown a line crossing at 7.0 GPa [35, 36]. The negative slope of the B_{2g} internal bending mode (~330 rel./cm at ambient pressure) is indicative of mode softening with increasing pressure. The line crossing is the intersection of the B_{2g} with the E_g rotational mode (~300 rel./cm at ambient pressure). For all materials in this study, the line crossing occurs between 7-8 GPa and occurs before the phase transformation. The line crossings are shown in Figure 3.2 and summarized in Table 3.2. Mode softening of xenotime structures has been attributed to the destabilization of its zircon structure which goes through anisotropic compression under hydrostatic pressure [39]. *Ab initio* calculations and experimental results have shown the PO₄ tetrahedron to be highly incompressible whereas the REO₈ dodecahedron is much more compressible and distorts anisotropically, thus the mode softening may correlate to

changes in the RE-O bonds.

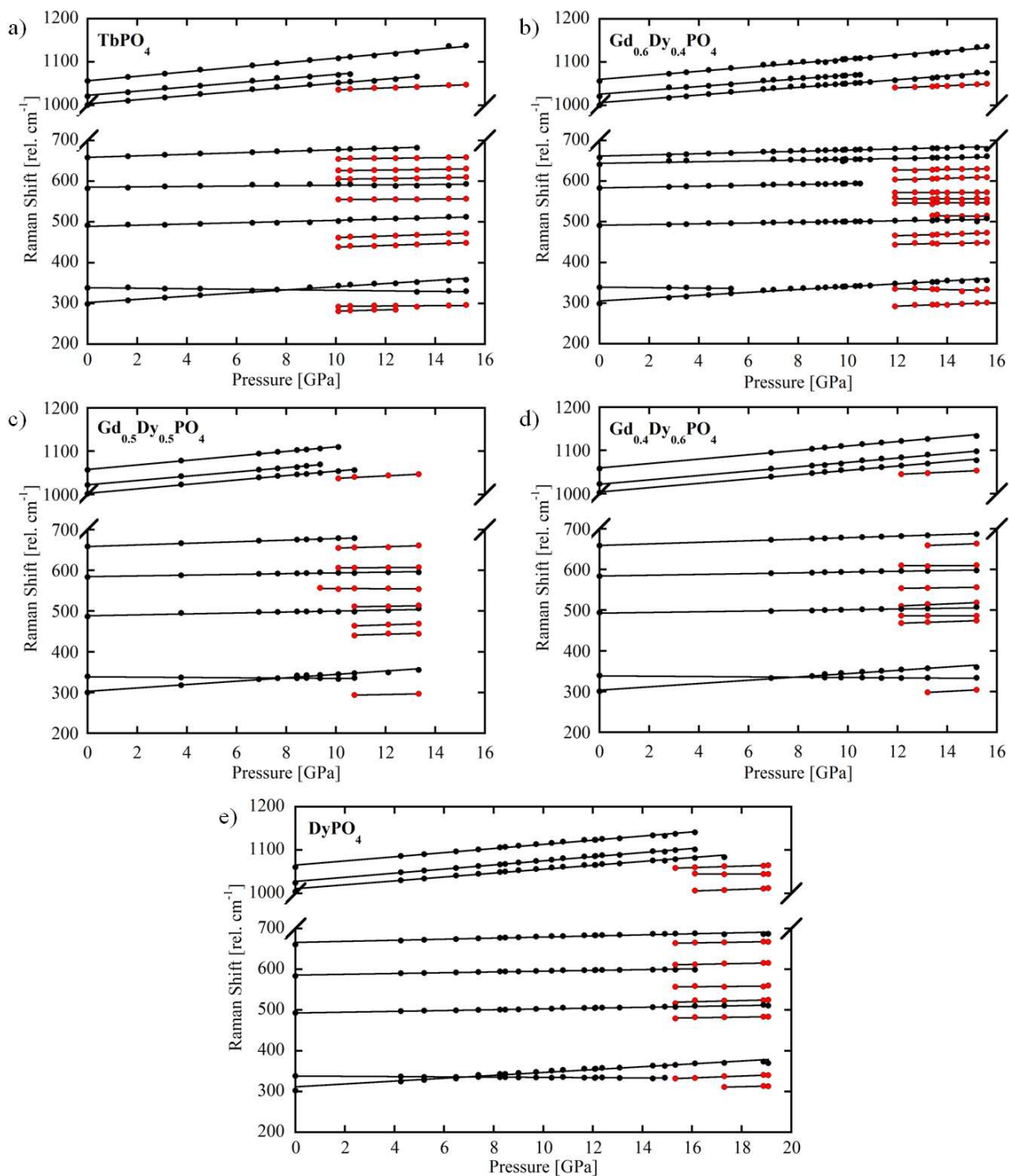


Figure 3.2: Raman modes as a function of pressure during compression. Initial xenotime phase modes are shown in black and new high-pressure phase modes are shown in red. At the onset of transformation a mostly full set of peaks appear.

Table 3.1: Xenotime Raman modes and slopes table of TbPO₄, DyPO₄, and Gd_xDy_(1-x)PO₄ solid solutions compared to those for TbPO₄, reported by Tatsi *et al.* [35].

TbPO ₄ (Tatsi, et al.) [35]			TbPO ₄		Gd _{0.6} Dy _{0.4} PO ₄		Gd _{0.5} Dy _{0.5} PO ₄		Gd _{0.4} Dy _{0.6} PO ₄		DyPO ₄	
Assignment	ω_0 [rel. cm ⁻¹]	$(\delta\omega/\delta P)_T$ [cm ⁻¹ /GPa]	ω_0 [rel. cm ⁻¹]	$(\delta\omega/\delta P)_T$ [cm ⁻¹ /GPa]	ω_0 [rel. cm ⁻¹]	$(\delta\omega/\delta P)_T$ [cm ⁻¹ /GPa]	ω_0 [rel. cm ⁻¹]	$(\delta\omega/\delta P)_T$ [cm ⁻¹ /GPa]	ω_0 [rel. cm ⁻¹]	$(\delta\omega/\delta P)_T$ [cm ⁻¹ /GPa]	ω_0 [rel. cm ⁻¹]	$(\delta\omega/\delta P)_T$ [cm ⁻¹ /GPa]
E _g	293	3.92	303	3.86	305	3.53	303	4.17	304	4.08	312	3.52
B _{2g}	331	-0.56	339	-0.65	339	-0.60	339	-0.42	339	-0.40	338	-0.33
A _{1g}	484	0.72	489	1.51	492	0.91	489	1.16	493	0.87	493	1.02
E _g	576	1.10	585	0.47	584	1.06	585	0.92	585	0.97	586	0.94
B _{1g}	649	1.98	659	1.82	662	1.47	659	1.93	659	1.88	666	1.35
A _{1g}	995	5.30	1003	4.78	1006	4.43	1003	5.10	1004	5.01	1011	4.48
E _g	1014	5.00	1023	4.80	1026	4.43	1022	4.98	1022	5.05	1028	4.76
B _{1g}	1049	5.30	1057	5.19	1060	4.70	1058	5.22	1060	5.08	1065	4.81

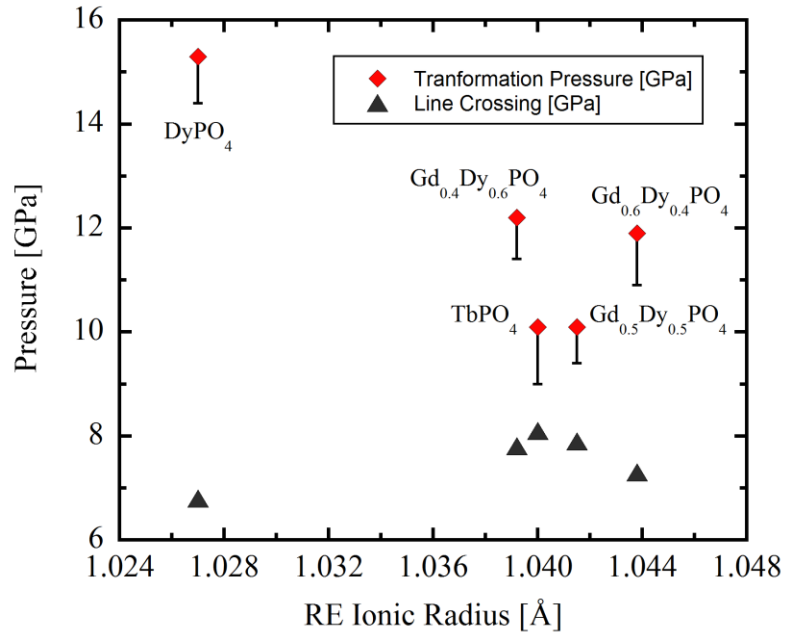


Figure 3.3: Experimental transformation pressures and line crossing pressures of xenotime REPO₄s measured in this study

The phase transformation pressures and line crossings of each material are shown in Figure 3.3 as a function of effective ionic radius. The transformation pressure data points in red represent the upper bound where the new phase was first observed. The error bars mark the preceding pressure interval over which transformation may have begun (also listed in Table 3.2).

Errors in pressure measurements may be present due to non-hydrostatic conditions above 10 GPa. For reference, a standard deviation of ± 1.0 GPa across the sample chamber is reported at 15 GPa [54] for the pressure medium used in this study. This potential source of error has been taken into consideration, but is not included explicitly in the graphical representation.

An intermediate anhydrite phase between the xenotime and monazite phases has been reported in similar material systems through XRD [31, 32, 42]. Previous Raman studies however have not reported this phase and there was no evidence suggesting an intermediate phase in these experiments. The Raman spectrum of anhydrite shares its primary modes with those of xenotime, thus Raman spectroscopy is not optimal for discerning between the two phases. Further characterization with *in situ* XRD is necessary for confirmation of the high-pressure monazite phase and in determining the presence of the intermediate anhydrite phase.

The transformation of polycrystalline TbPO_4 was observed at 10.1 GPa, agreeing with existing experimental data on single crystals (~ 9.5 GPa [35], 9.8 - 10.1 GPa [40]). Pure DyPO_4 transformed at 15.3 GPa. The $\text{Gd}_x\text{Dy}_{(1-x)}\text{PO}_4$ solid solutions transitioned near but slightly above the transformation pressure of TbPO_4 . Solid solutions $\text{Gd}_{0.4}\text{Dy}_{0.6}\text{PO}_4$ transformed at 12.2 GPa, $\text{Gd}_{0.5}\text{Dy}_{0.5}\text{PO}_4$ transformed at 10.1 GPa, and $\text{Gd}_{0.6}\text{Dy}_{0.4}\text{PO}_4$ transformed at 11.9 GPa. These results are summarized in Table 3.2. A decrease in transformation pressure with the addition of Gd from that of pure DyPO_4 is apparent, but relative differences between these three solid solutions weren't observed within the resolution of these experiments.

Table 3.2: Summary of experimental results for phase transformation pressures and line crossings. Errors reported are the resolutions of pressure increments indicating the previous pressure before transformation. (*Effective rare-earth radii of solid solutions are linear interpolations between the radii of Gd and Dy)

RE Ionic Radius [Å]	REPO ₄	Transformation Pressure [GPa]	Error (-) [GPa]	Line Crossing [GPa]
1.040	TbPO ₄	10.1	1.1	8.1
1.044*	Gd _{0.6} Dy _{0.4} PO ₄	11.9	1.0	7.3
1.042*	Gd _{0.5} Dy _{0.5} PO ₄	10.1	0.7	7.9
1.039*	Gd _{0.4} Dy _{0.6} PO ₄	12.2	0.8	7.8
1.027	DyPO ₄	15.3	0.9	6.8

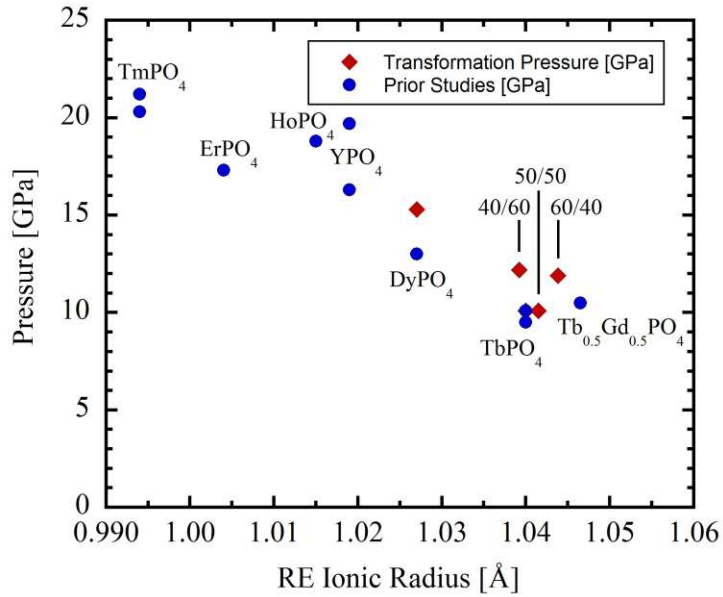


Figure 3.4: Experimental transformation pressures of xenotime REPO₄s from this study and previous studies

These experimental transformation pressures are consistent with existing research showing an overall decrease in transformation pressure with increasing rare-earth ionic radius, as shown in Figure 3.4. In this work, the addition of larger RE cations into a xenotime REPO₄ reduced the transformation pressure. Although the addition of Gd to DyPO₄ reduced its

transformation pressure, the relative differences between the solid solution transformation pressures were not resolved. In other studies, the addition of Gd to TbPO₄ did not reduce the transformation pressure (Tb_{0.5}Gd_{0.5}PO₄ transformed between 9 - 10.5 GPa) [42]. Thus far, a xenotime to monazite transformation pressure has not been observed below the 9 - 10 GPa range. This may be an indication of a lower limit to the transformation pressure of xenotime REPO₄s. Investigation into additional compositions of REPO₄ solid solutions with larger effective rare-earth radii could determine whether this limit exists.

Some xenotime REPO₄s have been observed to revert back to their initial phase upon decompression, while the transformations of other REPO₄s are irreversible. The decompression spectra for TbPO₄, DyPO₄, and the Gd_xDy_(1-x)PO₄ solid solutions are shown in Figure 3.5, alongside their initial xenotime spectrum for reference. The TbPO₄ phase transformation was observed to be non-reversible in this work and in previous studies [35, 40], retaining the high-pressure phase spectrum after decompression, as shown in Figure 3.5 (a). REPO₄s with smaller cation radii, further from the monazite/xenotime phase boundary such as ErPO₄ and YPO₄, transformed back to the xenotime structure [41]. The high-pressure transformations of the Gd_xDy_(1-x)PO₄ solid solutions, shown in Figures 3.5 (b),(c), and (d), were partially reversible, retaining the high-pressure peaks and reforming the xenotime peaks in the final spectrum. The reformation of the characteristic A_{1g} (~995 cm⁻¹) xenotime mode was not distinct but the recession of high-pressure phase modes was clearly evident. The phase transformation of DyPO₄ was reversible and transformed back to the xenotime phase upon decompression. Similar to the compression cycle, the receding of the A_g (~1033 cm⁻¹) monazite mode and the reformation of the A_{1g} (~995 cm⁻¹) xenotime mode is the strongest indicator of this transformation. Figure 3.5 (e) shows a final spectrum after decompression nearly identical to the initial spectrum.

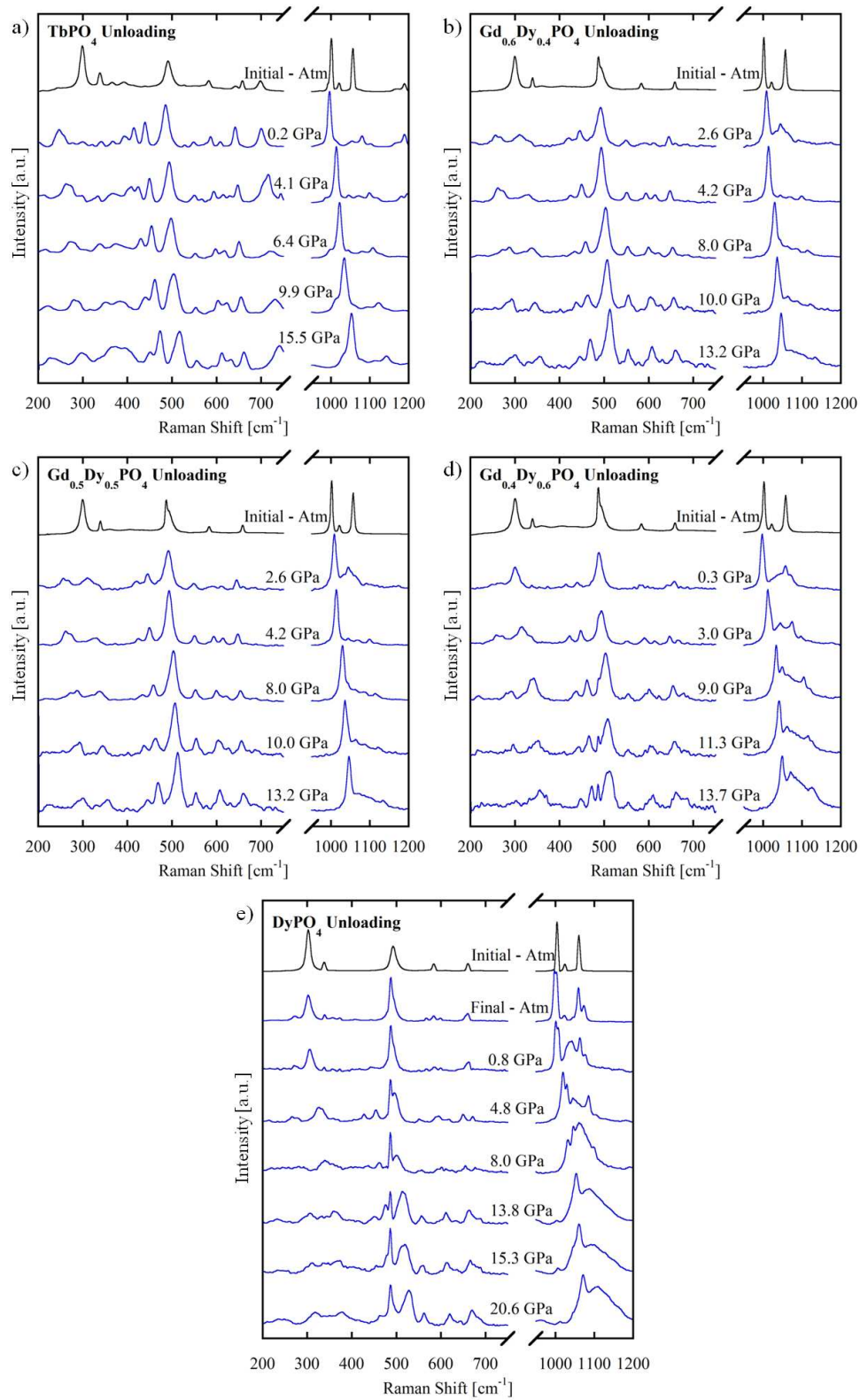


Figure 3.5: Decompression Raman spectra of TbPO₄ (a), Gd_{0.6}Dy_{0.4}PO₄ (b), Gd_{0.5}Dy_{0.5}PO₄ (c), Gd_{0.4}Dy_{0.6}PO₄ (d), and DyPO₄ (e).

Two low intensity peaks not associated with the xenotime phase remain at $\sim 290\text{ cm}^{-1}$ and $\sim 1080\text{ cm}^{-1}$. It is possible that these are localized metastable distortions in the lattice but further characterization techniques would be necessary for analysis. A large hysteresis was observed for DyPO_4 , with the first sign of transformation back to the xenotime phase occurring at 8 GPa (~ 7 GPa hysteresis). This is much larger than that reported for ErPO_4 and YPO_4 which have a 2 GPa pressure hysteresis [41]. Compared to ErPO_4 and YPO_4 , there would be a relatively smaller driving force for DyPO_4 to transform back into xenotime due to its meta-stability in the monazite phase as evidenced by its room-temperature polymorphism. Thus, the large hysteresis likely reflects a larger overpressure required to trigger the reverse transformation.

3.5 Manuscript – Conclusion

The high-pressure behavior of polycrystalline xenotime REPO_4 s (TbPO_4 , DyPO_4 , and $\text{Gd}_x\text{Dy}_{(1-x)}\text{PO}_4$ solid solutions ($x = 0.4, 0.5, 0.6$) was characterized in a diamond anvil cell using *in situ* Raman spectroscopy. Evidence for a pressure-induced phase transformation to a lower symmetry phase was found for all materials. The transformation spectra are consistent with the TbPO_4 transformation from xenotime to monazite and so it is likely that the high-pressure phase of DyPO_4 and the solid solutions are also the monazite monoclinic structure. Level crossing was observed in all structures, where mode softening with increasing pressure results in the overlapping of adjacent modes. This crossing occurred at roughly the same pressure for all materials at ~ 7 -8 GPa. The mode softening and subsequent line crossing has consistently preceded the phase transformation of REPO_4 xenotime-to-monazite transitions. $\text{Gd}_x\text{Dy}_{(1-x)}\text{PO}_4$ solid solutions demonstrate reduced transformation pressures compared to pure DyPO_4 , indicating a lowered transformation pressure with the substitution of a larger RE cation. These measurements of the fundamental phase transformation behavior under hydrostatic stress for

these REPO₄s can now be used to begin to understand potential relationships between phase transformation pressure and CMC fiber push-out stress in xenotime REPO₄ fiber coatings.

3.6 Manuscript – Acknowledgements

The researchers acknowledge Zachary McMullen and Ryan Plessinger for their assistance in preparing the polycrystalline samples and XRD, and the contributions of Dr. Jason Fish in the inauguration of this project. This research was funded by the National Science Foundation (NSF) under Award No.: DMR-1352499.

CHAPTER 4 CONCLUSIONS AND FUTURE WORK

REPO₄s are unique ceramic materials that plastically deform relatively easily compared to other ceramics with similar melting temperatures (above 2000°C) which has led to further investigation of their mechanical properties for applications in structural ceramics. The utilization of REPO₄ fiber coatings in CMCs has demonstrated desirable mechanical responses that increase the fracture toughness and strength of the composite system. The coatings remain chemically stable at high temperatures and deflect cracks around the dispersed fibers, following the weakly bonded interface. Furthermore, certain xenotime REPO₄ coatings promote fiber sliding which strengthens the bridging mechanism that shields the crack tip and inhibits crack propagation. This composition of Gd_{0.4}Dy_{0.6}PO₄ was shown to have a lower average fiber push-out stress than DyPO₄ and monazite LaPO₄ fiber coatings [31]. This difference was attributed to transformation plasticity and volume reduction in small regions of the coating that phase transformed.

Prior to this study, the phase transformation behavior of DyPO₄ and Gd_xDy_(1-x)PO₄ solid solutions hadn't been experimentally documented. Therefore, powder samples were synthesized by aqueous precipitation and processed for high-pressure experiments. Hydrostatic compression in DAC was conducted and analyzed using *in situ* Raman spectroscopy. The onset of phase transformation for DyPO₄ occurred at a pressure of 15.3 GPa and underwent a reversible phase transformation, returning to the xenotime phase after decompression. The transformation pressures of the solid solutions (Gd_xDy_(1-x)PO₄) were in the range of 10 – 12 GPa. The Gd_xDy_(1-x)PO₄ solid solutions yielded partially reversible phase transformations, retaining some of the high-pressure phase spectrum while reforming xenotime peaks during decompression. The substitution of Gd into DyPO₄ decreased the transformation pressure relative to pure DyPO₄.

In advancing this area of research, there are different avenues to be pursued. The effects of reversibility in the performance of CMC fiber coatings are not well understood but may have an impact. Further experimental characterization of the structure under high pressure with *in situ* XRD could provide additional details of the lattice compression and phase transformations. Mechanical properties of these materials could be derived from the results. Multiple combinations of rare-earth elements could be synthesized into REPO₄ solid solutions. High-pressure characterization across a variety of compositions would contribute to understanding the transformation behavior of these materials. Density functional theory (DFT) calculations of the electronic structure could simulate the effects of substituting rare-earth cations in place of others.

Additionally, the intermediate anhydrite phase needs to be investigated further. The pressures reported were for the xenotime-to-monazite phase transformations. With no monazite transformation pressures below 9.5 GPa, it would be interesting to measure the xenotime-to-anhydrite phase transformations of the REPO₄s in this study, which are currently unknown. Perhaps the effects on transformation behavior are different for this transformation. XRD measurements are necessary to observe this transformation.

REFERENCES CITED

- [1] G. M. Begun, G. W. Beall, L. A. Boatner, and W. J. Gregor, "Raman-spectra of the rare-earth ortho-phosphates," *Journal of Raman Spectroscopy*, vol. 11, pp. 273-278, 1981.
- [2] R. Elliott, R. Harley, W. Hayes, and S. Smith, "Raman scattering and theoretical studies of Jahn-Teller induced phase transitions in some rare-earth compounds," in *Proceedings of the Royal Society of London A: Mathematical, Physical and Engineering Sciences*, 1972, pp. 217-266.
- [3] Y. X. Ni, J. M. Hughes, and A. N. Mariano, "Crystal-chemistry of the monazite and xenotime structures," *American Mineralogist*, vol. 80, pp. 21-26, Jan-Feb 1995.
- [4] A. T. Aldred, "Cell volumes of AP_4O_{10} , AVO_4 , and $AnBO_4$ compounds, where $A = Sc, Y, La-Lu$," *Acta Crystallographica Section B-Structural Science*, vol. 40, pp. 569-574, 1984.
- [5] E. E. Boakye, P. Mogilevsky, R. S. Hay, and G. E. Fair, "Synthesis and phase composition of lanthanide phosphate nanoparticles $LnPO_4$ ($Ln=La, Gd, Tb, Dy, Y$) and solid solutions for fiber coatings," *Journal of the American Ceramic Society*, vol. 91, pp. 3841-3849, 2008.
- [6] L. A. Boatner, M. M. Abraham, and M. Rappaz, "Analogues of monazite for the storage of radioactive-wastes," *Transactions of the American Nuclear Society*, vol. 35, pp. 186-187, 1980.
- [7] L. A. Boatner, G. W. Beall, M. M. Abraham, C. B. Finch, P. G. Huray, and M. Rappaz, "Monazite and Other Lanthanide Orthophosphates as Alternate Actinide Waste Forms," in *Scientific Basis for Nuclear Waste Management*, C. J. M. Northrup, Ed., ed Boston, MA: Springer US, 1980, pp. 289-296.
- [8] A. Meldrum, L. A. Boatner, W. J. Weber, and R. C. Ewing, "Radiation damage in zircon and monazite," *Geochimica Et Cosmochimica Acta*, vol. 62, pp. 2509-2520, Jul 1998.
- [9] O. Terra, N. Clavier, N. Dacheux, and R. Podor, "Preparation and characterization of lanthanum-gadolinium monazites as ceramics for radioactive waste storage," *New Journal of Chemistry*, vol. 27, pp. 957-967, 2003.
- [10] H. Schlenz, J. Heuser, A. Neumann, S. Schmitz, and D. Bosbach, "Monazite as a suitable actinide waste form," *Zeitschrift für Kristallographie-Crystalline Materials*, vol. 228, pp. 113-123, 2013.
- [11] M. R. Winter and D. R. Clarke, "Oxide materials with low thermal conductivity," *Journal of the American Ceramic Society*, vol. 90, pp. 533-540, Feb 2007.
- [12] A. Du, C. Wan, Z. Qu, and W. Pan, "Thermal Conductivity of Monazite-Type $REPO_4$ ($RE=La, Ce, Nd, Sm, Eu, Gd$)," *Journal of the American Ceramic Society*, vol. 92, pp. 2687-2692, 2009.

- [13] U. Sasum, M. Kloss, A. Rohmann, L. Schwarz, and D. Haberland, "Optical properties of some rare earth and alkaline rare earth orthophosphates," *Journal of Luminescence*, vol. 72-4, pp. 255-256, Jun 1997.
- [14] A. A. Kaminskii, M. Bettinelli, A. Speghini, H. Rhee, H. J. Eichler, and G. Mariotto, "Tetragonal YPO₄ - a novel SRS-active crystal," *Laser Physics Letters*, vol. 5, pp. 367-374, May 2008.
- [15] F. Meiser, C. Cortez, and F. Caruso, "Biofunctionalization of fluorescent rare-earth-doped lanthanum phosphate colloidal nanoparticles," *Angewandte Chemie-International Edition*, vol. 43, pp. 5954-5957, 2004.
- [16] J. B. Davis, D. B. Marshall, and P. E. D. Morgan, "Monazite-containing oxide/oxide composites," *Journal of the European Ceramic Society*, vol. 20, pp. 583-587, 2000.
- [17] P. Y. Lee, M. Imai, and T. Yano, "Fracture behavior of monazite-coated alumina fiber-reinforced alumina-matrix composites at elevated temperature," *Journal of the Ceramic Society of Japan*, vol. 112, pp. 628-633, Dec 2004.
- [18] P. E. D. Morgan, D. B. Marshall, and R. M. Housley, "High-temperature stability of monazite-alumina composites," *Materials Science and Engineering a-Structural Materials Properties Microstructure and Processing*, vol. 195, pp. 215-222, Jun 1 1995.
- [19] K. A. Keller, T. I. Mah, T. A. Parthasarathy, E. E. Boakye, P. Mogilevsky, and M. K. Cinibulk, "Effectiveness of monazite coatings in oxide/oxide composites after long-term exposure at high temperature," *Journal of the American Ceramic Society*, vol. 86, pp. 325-332, Feb 2003.
- [20] P. Y. Lee, M. Imai, and T. Yano, "Effects of sintering condition on mechanical properties of monazite-coated alumina-fiber/alumina-matrix composites fabricated by hot-pressing," *Journal of the Ceramic Society of Japan*, vol. 112, pp. 29-34, Jan 2004.
- [21] P. E. D. Morgan and D. B. Marshall, "Ceramic composites of monazite and alumina," *Journal of the American Ceramic Society*, vol. 78, pp. 1553-1563, Jun 1995.
- [22] D. B. Marshall, "An Indentation Method for Measuring Matrix-Fiber Frictional Stresses in Ceramic Composites," *Journal of the American Ceramic Society*, vol. 67, pp. C259-C260, 1984.
- [23] D. B. Marshall and A. G. Evans, "Failure Mechanisms in Ceramic-Fiber Ceramic-Matrix Composites," *Journal of the American Ceramic Society*, vol. 68, pp. 225-231, 1985.
- [24] A. G. Evans and D. B. Marshall, "The Mechanical-Behavior of Ceramic Matrix Composites," *Acta Metallurgica*, vol. 37, pp. 2567-2583, Oct 1989.
- [25] P. F. Becher and T. N. Tiegs, "Toughening Behavior Involving Multiple Mechanisms - Whisker Reinforcement and Zirconia Toughening," *Journal of the American Ceramic Society*, vol. 70, pp. 651-654, Sep 1987.

- [26] H. C. Cao, E. Bischoff, O. Sbaizero, M. Ruhle, A. G. Evans, D. B. Marshall, *et al.*, "Effect of interfaces on the properties of fiber-reinforced ceramics," *Journal of the American Ceramic Society*, vol. 73, pp. 1691-1699, Jun 1990.
- [27] J. B. Davis, R. S. Hay, D. B. Marshall, P. E. D. Morgan, and A. Sayir, "Influence of interfacial roughness on fiber sliding in oxide composites with La-monazite interphases," *Journal of the American Ceramic Society*, vol. 86, pp. 305-316, Feb 2003.
- [28] D. H. Kuo, W. M. Kriven, and T. J. Mackin, "Control of interfacial properties through fiber coatings: Monazite coatings in oxide-oxide composites," *Journal of the American Ceramic Society*, vol. 80, pp. 2987-2996, Dec 1997.
- [29] W. A. Curtin, J. I. Eldridge, and G. V. Srinivasan, "Push-out tests on a new silicon-carbide reaction-bonded silicon-carbide ceramic-matrix composite," *Journal of the American Ceramic Society*, vol. 76, pp. 2300-2304, Sep 1993.
- [30] W. Yang, A. Kohyama, T. Noda, Y. Katoh, T. Hinoki, H. Araki, *et al.*, "Interfacial characterization of CVI-SiC/SiC composites," *Journal of Nuclear Materials*, vol. 307, pp. 1088-1092, Dec 2002.
- [31] R. S. Hay, E. E. Boakye, P. Mogilevsky, G. E. Fair, T. A. Parthasarathy, and J. E. Davis, "Transformation plasticity in $(\text{Gd}_x\text{Dy}_{1-x})\text{PO}_4$ fiber coatings during fiber push out," *Journal of the European Ceramic Society*, vol. 96, pp. 1586-1595, May 2013.
- [32] R. S. Hay, P. Mogilevsky, and E. Boakye, "Phase transformations in xenotime rare-earth orthophosphates," *Acta Materialia*, vol. 61, pp. 6933-6947, Oct 2013.
- [33] E. Stavrou, A. Tatsi, E. Salpea, Y. C. Boulmetis, A. G. Kontos, Y. S. Raptis, *et al.*, "Raman study of zircon-structured RPO4 (R = Y, Tb, Er, Tm) phosphates at high pressures," *Joint 21st Airapt and 45th Ehprg International Conference on High Pressure Science and Technology*, vol. 121, 2008.
- [34] E. Stavrou, A. Tatsi, C. Raptis, I. Efthimiopoulos, K. Syassen, A. Munoz, *et al.*, "Effects of pressure on the structure and lattice dynamics of TmPO4: Experiments and calculations," *Physical Review B*, vol. 85, Jan 23 2012.
- [35] A. Tatsi, E. Stavrou, Y. C. Boulmetis, A. G. Kontos, Y. S. Raptis, and C. Raptis, "Raman study of tetragonal TbPO(4) and observation of a first-order phase transition at high pressure," *Journal of Physics-Condensed Matter*, vol. 20, Oct 22 2008.
- [36] A. G. Kontos, E. Stavrou, V. Malamos, Y. S. Raptis, and C. Raptis, "High pressure Raman study of DyPO4 at room and low temperatures," *Physica Status Solidi B-Basic Solid State Physics*, vol. 244, pp. 386-391, Jan 2007.
- [37] K. M. Heffernan, N. L. Ross, E. C. Spencer, and L. A. Boatner, "The structural response of gadolinium phosphate to pressure," *Journal of Solid State Chemistry*, vol. 241, pp. 180-186, 2016.

- [38] F. X. Zhang, J. W. Wang, M. Lang, J. M. Zhang, R. C. Ewing, and L. A. Boatner, "High-pressure phase transitions of ScPO₄ and YPO₄," *Physical Review B*, vol. 80, Nov 2009.
- [39] O. Gomis, B. Lavina, P. Rodriguez-Hernandez, A. Munoz, R. Errandonea, D. Errandonea, *et al.*, "High-pressure structural, elastic, and thermodynamic properties of zircon-type HoPO₄ and TmPO₄," *J Phys Condens Matter*, vol. 29, p. 095401, Mar 08 2017.
- [40] J. Lopez-Solano, P. Rodriguez-Hernandez, A. Munoz, O. Gomis, D. Santamaria-Perez, D. Errandonea, *et al.*, "Theoretical and experimental study of the structural stability of TbPO₄ at high pressures," *Physical Review B*, vol. 81, Apr 1 2010.
- [41] R. Lacomba-Perales, D. Errandonea, Y. Meng, and M. Bettinelli, "High-pressure stability and compressibility of A PO₄ (A= La, Nd, Eu, Gd, Er, and Y) orthophosphates: An x-ray diffraction study using synchrotron radiation," *Physical Review B*, vol. 81, p. 064113, 2010.
- [42] O. Tschauner, S. V. Ushakov, A. Navrotsky, and L. A. Boatner, "Phase transformations and indications for acoustic mode softening in Tb-Gd orthophosphate," *Journal of Physics: Condensed Matter*, vol. 28, p. 035403, 2016.
- [43] P. P. Bose, R. Mittal, S. L. Chaplot, C. K. Loong, and L. A. Boatner, "Inelastic neutron scattering, lattice dynamics, and high-pressure phase stability of zircon-structured lanthanide orthophosphates," *Physical Review B*, vol. 82, Sep 22 2010.
- [44] R. Mittal, S. L. Chaplot, N. Choudhury, and C. K. Loong, "Inelastic neutron scattering, lattice dynamics and high-pressure phase stability in LuPO₄ and YbPO₄," *Journal of Physics-Condensed Matter*, vol. 19, Nov 7 2007.
- [45] J. Feng, B. Xiao, R. Zhou, and W. Pan, "Anisotropy in elasticity and thermal conductivity of monazite-type REPO₄ (RE = La, Ce, Nd, Sm, Eu and Gd) from first-principles calculations," *Acta Materialia*, vol. 61, pp. 7364-7383, Nov 2013.
- [46] J. Ruiz-Fuertes, A. Hirsch, A. Friedrich, B. Winkler, L. Bayarjargal, W. Morgenroth, *et al.*, "High-pressure phase of LaPO₄ studied by x-ray diffraction and second harmonic generation," *Physical Review B*, vol. 94, Oct 28 2016.
- [47] R. T. Shannon, "Revised effective ionic radii and systematic studies of interatomic distances in halides and chalcogenides," *Acta Crystallographica Section A: Crystal Physics, Diffraction, Theoretical and General Crystallography*, vol. 32, pp. 751-767, 1976.
- [48] F. X. Zhang, M. Lang, R. C. Ewing, J. Lian, Z. W. Wang, J. Hu, *et al.*, "Pressure-induced zircon-type to scheelite-type phase transitions in YbPO₄ and LuPO₄," *Journal of Solid State Chemistry*, vol. 181, pp. 2633-2638, Oct 2008.
- [49] R. S. Hay, E. E. Boakye, and P. Mogilevsky, "Transformation plasticity in TbPO₄ and (Gd,Dy)PO₄ orthophosphates during indentation of polycrystalline specimens," *Journal*

of the European Ceramic Society, vol. 34, pp. 773-781, Mar 2014.

- [50] H. K. Mao, J. Xu, and P. M. Bell, "Calibration of the ruby pressure gauge to 800-kbar under quasi-hydrostatic conditions," *Journal of Geophysical Research-Solid Earth and Planets*, vol. 91, pp. 4673-4676, Apr 10 1986.
- [51] C. S. Zha, H. K. Mao, and R. J. Hemley, "Elasticity of MgO and a primary pressure scale to 55 GPa," *Proceedings of the National Academy of Sciences of the United States of America*, vol. 97, pp. 13494-13499, Dec 5 2000.
- [52] P. E. D. Morgan and D. B. Marshall, "Ceramic composites of monazite and alumina," *Journal of the American Ceramic Society*, vol. 78, pp. 2574-2574, Sep 1995.
- [53] A. P. Gysi, D. Harlov, D. Costa, and A. E. Williams-Jones, "Experimental determination of the high temperature heat capacity of a natural xenotime-(Y) solid solution and synthetic DyPO₄ and ErPO₄ endmembers," *Thermochimica Acta*, vol. 627, pp. 61-67, Mar 20 2016.
- [54] S. Klotz, J. C. Chervin, P. Munsch, and G. Le Marchand, "Hydrostatic limits of 11 pressure transmitting media," *Journal of Physics D-Applied Physics*, vol. 42, Apr 7 2009.